Check for updates

Recent advances in BiVO$_4$-based heterojunction photocatalysts for energy and environmental applications

Yajie Bai,*[a] Zhenyuan Fang,[c] Yuning Fang,[a] Chenxiao Lin, [iD][a] Hongye Bai [iD][b] and Weiqiang Fan [iD] *[b]

Photocatalytic technology offers a promising solution by efficiently converting solar energy into chemical energy and addressing environmental pollution. BiVO$_4$ is a promising semiconductor photocatalytic material due to its narrow band gap, good visible light response, and non-toxicity. Recently, there has been significant interest in developing BiVO$_4$-based heterojunction photocatalysts to overcome the challenges of rapid recombination rate of photogenerated charge carriers and insufficient electron transport capacity in pure BiVO$_4$. However, a comprehensive and systematic summary of the role of BiVO$_4$-based heterojunction catalysts in improving photocatalytic performance is lacking. This review covers the mechanisms, challenges, and classification of BiVO$_4$-based heterojunction photocatalysis. It also summarizes recent advancements in using these photocatalysts for energy and environmental applications, such as water splitting, nitrogen fixation, carbon dioxide reduction, pollutant degradation, *etc.* Perspectives on the existing challenges, potential solutions, and prospects of BiVO$_4$-based heterojunction photocatalysts are outlined, aiming to offer valuable insights to accelerate their commercialization as high-performance photocatalysts.

[a] *College of New Energy, Ningbo University of Technology, Ningbo, 315336, P. R. China. E-mail: byj@nbut.edu.cn*
[b] *School of Chemistry and Chemical Engineering, Jiangsu University, Zhenjiang, 212013, P. R. China. E-mail: fwq4993329@ujs.edu.cn*
[c] *School of Chemistry, Beihang University, Beijing, 100191, P. R. China*

1. Introduction

Rapid industrial development and continuous global population growth have accelerated energy shortages and environmental pollution.[1] Moreover, global industrialization has driven excessive consumption of traditional fossil fuels, such as oil, coal, and natural gas, leading to significant harmful

Yajie Bai

Dr Yajie Bai received her BSc degree in Chemistry from Longdong University in 2017 and then joined Jiangsu University, where she earned her PhD degree in Environmental Science and Engineering in 2023. She is now working as an assistant professor at Ningbo University of Technology. Her current research interests mainly focus on photoelectrochemical technologies for water splitting and nitrogen fixation.

Weiqiang Fan

Prof. Weiqiang Fan received his BSc degree in Chemistry from Inner Mongolia University in 2006 and then joined Changchun Institute of Applied Chemistry, Chinese Academy of Sciences (CAS), where he earned his PhD degree in inorganic chemistry in 2011. He is now working as a professor at Jiangsu University. His current research interests mainly focus on photoelectrochemical technologies for biomass conversion, water splitting, and nitrogen fixation.

waste emissions that threaten the ecological environment essential for human survival.[2] Therefore, it is crucial to develop environmentally friendly and renewable green technologies for both energy production and environmental remediation, addressing the growing challenges of energy shortages and environmental pollution.[3] In this case, photocatalytic technology has garnered significant attention as an effective solution to energy and environmental challenges due to its cost-effectiveness, eco-friendliness, mild reaction conditions, and lack of secondary pollution.[4,5] This technology enables the photocatalytic processes of water splitting,[6] nitrogen fixation,[7] and carbon dioxide (CO_2) reduction,[8] converting renewable solar energy into valuable, storable chemical energy. Furthermore, photocatalysts can directly harness solar energy to activate semiconductor materials, generating reactive species that effectively remove harmful and toxic pollutants.[9,10] Since 1972, after Fujishima and Honda discovered the water-splitting phenomenon using TiO_2 photocatalysis,[11] numerous semiconductor materials have been developed and widely applied in various photocatalytic reactions. Despite their advantages, photocatalytic reactions face practical application challenges due to the intrinsic limitations of photocatalysts, including low efficiency and instability from rapid recombination of photogenerated charge carriers.[12,13] Therefore, designing efficient and sustainable semiconductor photocatalysts is crucial.

TiO_2 is an outstanding photocatalyst due to its high photocatalytic activity, excellent chemical stability, non-toxicity, and cost-effectiveness.[14,15] However, conventional anatase-phase TiO_2 photocatalysts are active only under ultraviolet (UV) light (wavelength < 387 nm) due to their wide bandgap of 3.2 eV.[16,17] Since visible light dominates the solar spectrum, while UV light accounts for less than 4%,[18] developing visible-light-responsive photocatalysts is crucial for efficient solar energy utilization. In this case, $BiVO_4$ has emerged as a promising photocatalytic semiconductor material due to its favorable response to visible light.[19] $BiVO_4$ has significant potential in various catalytic applications, including water splitting, organic pollutant degradation, CO_2 reduction, and nitrate reduction.[20–22] However, $BiVO_4$ faces several challenges like low photogenerated charge separation efficiency, slow water oxidation kinetics, and rapid recombination of photogenerated electron–hole pairs.[23,24] These challenges limit its practical applications, making the development of efficient $BiVO_4$-based photocatalysts a critical research focus. To enhance the performance of $BiVO_4$, researchers have employed various techniques, including ion doping, crystal facet regulation, morphology control, and microporous/mesoporous structures construction.[25–27] Among these strategies, developing $BiVO_4$-based heterojunction catalysts by combining $BiVO_4$ with semiconductors that possess complementary properties and matching energy levels has proven effective in improving photocatalytic performance.[28,29] $BiVO_4$-based heterojunction catalysts enhance charge separation efficiency, reduce the recombination rate of photogenerated electron–hole pairs, and introduce new properties through synergistic effects with other components.[30,31] Rational design of $BiVO_4$-based heterojunction catalysts presents a promising approach for developing efficient

visible-light-driven photocatalysts, thereby advancing environmental and energy applications. Although $BiVO_4$-based heterojunction catalysts have been developed for photocatalysis, there is a lack of a comprehensive and systematic summary of their role in enhancing photocatalytic performance.

Herein, we provide a comprehensive overview of the photocatalytic mechanism, design strategies and types of $BiVO_4$-based heterojunction photocatalysts. $BiVO_4$-based heterojunction photocatalysts can be categorized into five types based on the mechanisms of separation and transport of photogenerated electron–hole pairs: traditional heterojunctions (type I, type II, and type III), Schottky heterojunctions, Z-scheme heterojunctions, and S-scheme heterojunctions. The applications of $BiVO_4$-based heterojunction photocatalysts in energy and environmental processes, including water splitting, nitrogen fixation, CO_2 reduction, H_2O_2 synthesis, pollutant degradation, HCHO removal, and bacterial inactivation, are summarized. This work also highlights the advantages of $BiVO_4$-based heterojunctions in photocatalytic processes, focusing on their construction methods and efficient photogenerated electron–hole separation and transfer mechanisms. It is expected to provide valuable guidance for developing highly efficient heterojunction photocatalysts and to inspire advancements in practical applications across various fields.

2. Fundamentals of photocatalysis

2.1 Mechanisms of photocatalytic activity in $BiVO_4$-based heterojunctions

Photocatalytic processes involve a complex reaction mechanism with several complementary and indispensable steps, as shown in Fig. 1. Firstly, light absorption by the semiconductor is a crucial step in photocatalytic reactions. When the photocatalyst is irradiated with photons of energy equal to or greater than its bandgap (E_g), electrons (e^-) in the valence band (VB) are excited and transition to the conduction band (CB), forming photogenerated electron–hole pairs (h^+). Subsequently, these photogenerated charge carriers separate and migrate to the surface or interface of the semiconductor, facilitating redox
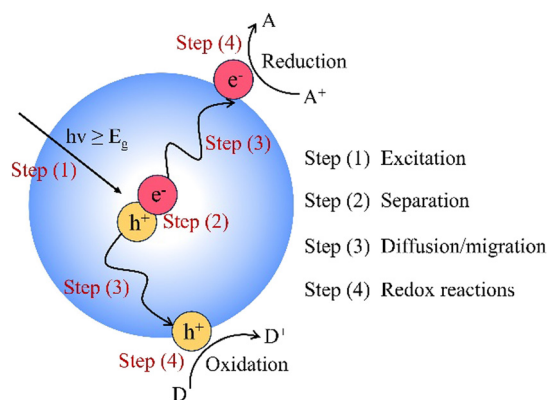

Fig. 1 Schematic illustration of the photocatalytic processes (*hv*: illumination; E_g: bandgap).

reactions and generating radicals such as $^\bullet OH$, $^\bullet O_2^-$, and H^+. During this process, the recombination of electron–hole pairs can reduce photocatalytic efficiency, as it leads to energy loss in the form of heat instead of driving the reaction. Therefore, it is crucial for the photogenerated electron–hole pairs to selectively transfer to the surface of the photocatalyst to initiate redox reactions, rather than recombine and produce waste heat. Additionally, the adsorption of reactants and desorption of products are also crucial for continuous photocatalytic reaction.[32,33] Improving these processes is essential for enhancing photocatalytic performance. Optimizing photocatalyst design and operational conditions can effectively increase the separation efficiency of photogenerated charge carriers, promote the efficient adsorption of reactants, and accelerate product desorption, leading to more efficient photocatalytic reactions.

2.2 Challenges of photocatalysis

Despite the significant potential of photocatalytic technologies, their practical implementation still faces several challenges: (1) slow reaction kinetics: photocatalytic processes involve several steps, including excitation, separation, transport, and surface reaction of photogenerated charge carriers. These steps occur at a slow rate, resulting in low efficiency, especially in complex reactions like CO_2 and NO_3^- reduction, where multiple interdependent steps further slow the reaction rate.[34] (2) Wide bandgap limiting light absorption: the performance of photocatalysts relies on effective light capture, charge separation, and charge transport. Many commonly used photocatalysts, such as TiO_2, have wide bandgaps, limiting their absorption in the visible light range and reducing overall photocatalytic efficiency.[35] (3) High recombination rates of photogenerated electrons and holes: photogenerated electrons and holes must be effectively separated and transported to the catalytic surface for redox reactions. However, due to inefficient charge separation and transport, most photogenerated charge carriers recombine, reducing catalytic efficiency and potentially leading to catalyst degradation. Therefore, developing efficient and stable photocatalysts remains a critical challenge in the field.[36]

2.3 Advantages of BiVO$_4$-based heterojunction photocatalysts

To address the challenges of photocatalysts, the development of advanced photocatalysts, such as BiVO$_4$-based heterojunction photocatalysts has gained significant attention due to their favorable response to visible light. The main advantages of BiVO$_4$-based heterojunction catalysts are listed as follows: (1) improved reaction kinetics. BiVO$_4$-based heterojunctions can provide more active sites and increase the surface area available for reactions, reducing reaction barriers and accelerating rate-limiting steps. Optimized charge distribution at the interface of BiVO$_4$-based heterojunctions facilitates the adsorption and activation of reactants, enhancing the overall reaction kinetics.[37] (2) Expanded light absorption spectrum. Combining BiVO$_4$ with other semiconductors of different bandgaps broadens the light absorption spectrum, enabling efficient absorption of both UV and visible light, thus enhancing overall photocatalytic efficiency.[38] (3) Enhanced charge separation

and transport efficiency. The interfaces of BiVO$_4$-based heterojunctions can create built-in electric fields that promote effective separation of photogenerated electrons and holes, reducing recombination. When the band structures of the two materials are aligned, electrons can be directed to one material, while holes migrate to the other, further improving charge utilization. Additionally, BiVO$_4$-based heterojunctions can provide multiple pathways for electron transport, accelerating charge migration and enhancing charge separation and transport efficiency.[39] By enhancing catalytic activity, optimizing light absorption, and improving charge separation and transport efficiency, BiVO$_4$-based heterojunctions offer a practical solution to the challenges faced by photocatalytic technologies. Rational design and synthesis of BiVO$_4$-based heterojunctions hold great promise for significantly improving the performance and practical applicability of photocatalytic systems.

3. Classification of BiVO$_4$-based heterojunction photocatalysts

BiVO$_4$ forms a heterojunction with semiconductors that have compatible energy band structures, enabling rapid separation of electrons and holes in the valence band and conduction band. This prevents recombination of electron–hole pairs and enhances the photocatalytic efficiency of BiVO$_4$. According to the various charge separation mechanisms (Fig. 2), BiVO$_4$-based heterojunctions are categorized into: (1) traditional heterojunctions (type I, type II, and type III), (2) Schottky heterojunctions, (3) Z-scheme heterojunctions, and (4) S-scheme heterojunctions.

3.1 Traditional heterojunctions

Type I heterojunction photocatalysts consist of two semiconductors: semiconductor A, with an E_g fully within the E_g of semiconductor B, as illustrated in Fig. 2a.[40,41] Under illumination, photogenerated electrons transfer from the CB of semiconductor B to the CB of semiconductor A due to the potential difference, while photogenerated holes migrate from the VB of semiconductor B to the VB of semiconductor A. Photogenerated holes and electrons in semiconductor A participate in the redox reactions of photocatalysis.[42,43] This charge transfer mechanism may extend the lifetimes of photogenerated charges.[44] However, in type I heterojunctions, photogenerated electrons and holes transfer and accumulate in the same semiconductor, leading to insufficient spatial separation of the charge carriers. This lowers the potential of charge carriers for redox reactions, making the redox processes thermodynamically unfavorable.[5,45] The limited spatial separation results in a high probability of recombination, which diminishes the overall photocatalytic efficiency. Additionally, the energy band alignment in type I heterojunctions can be influenced by factors such as temperature and material defects, further complicating the charge transfer dynamics.

In type II heterojunction photocatalysts, the conduction and VB positions of semiconductors A and B are staggered,
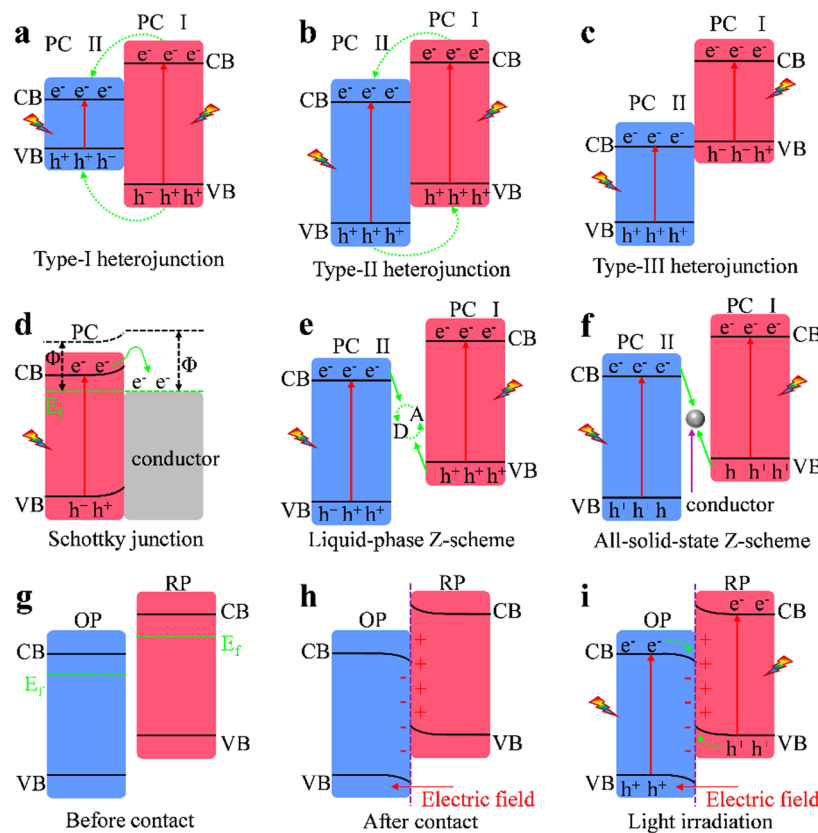
Fig. 2 Schematic diagram of different types of heterojunctions photocatalysts. (a) Type I, (b) type II, (c) type III, (d) Schottky heterojunction, (e) liquid-phase Z-scheme, (f) all-solid-state Z-scheme, and S-Scheme, (g) before contact, (h) after contact, and (i) light irradiation photocatalytic systems. The labels D and A denote the electron donor and acceptor in (e), respectively.

as shown in Fig. 2b.[46,47] Under light excitation, photogenerated electrons migrate from the higher energy CB of semiconductor B to the lower energy CB of semiconductor A, enriching in A. Simultaneously, photogenerated holes migrate from the VB of semiconductor A to the VB of semiconductor B, enriching in B, thereby achieving spatial separation of charge carriers.[48] This process significantly reduces the electron–hole pair recombination and extends the lifetime of the electrons.[49,50] The staggered band alignment in type II heterojunctions not only facilitates effective charge separation but also enhances the driving force for redox reactions, as the energy levels of the charge carriers are more favorable for participating in photocatalytic processes. However, this charge transfer mechanism has limitations. Similar to type I heterojunctions, the photogenerated charge carriers have lower redox potentials, reducing their redox capability in photocatalytic reactions.[50] Furthermore, photogenerated electron accumulation in the CB of semiconductor A inhibits electron injection from semiconductor B, slowing the migration of the photogenerated charge carriers.[51] This accumulation can lead to a saturation effect, where the rate of charge transfer becomes limited by the available states in the conduction band. Additionally, energy losses due to non-radiative recombination and thermalization further limit the effectiveness of photocatalytic reactions,[52] making type II heterojunction photocatalysts challenging in terms of thermodynamics, kinetics, and

energy efficiency. Type III heterojunctions are characterized by a broken band alignment between the two semiconductors that exhibit no overlap in their E_g (Fig. 2c).[53] This configuration allows for the combination of various semiconductors, including those with strong redox abilities and broad light-response ranges. In type III heterojunctions, the lack of overlap in energy bands creates unique charge transfer pathways that can potentially enhance photocatalytic activity by allowing for the utilization of a wider range of light wavelengths. This is particularly advantageous for applications requiring high energy efficiency across different spectral regions. These features give type III heterojunctions the potential to overcome the trade-offs between light response range and redox potential in type II heterojunctions.[54] However, high energy barriers hinder charge transfer and separation across the bands, posing challenges for photocatalysis and photothermal catalysis applications.[55] The presence of these energy barriers can lead to inefficient charge carrier dynamics, where the photogenerated electrons and holes may recombine before they can participate in catalytic reactions. This recombination can significantly reduce the overall efficiency of the photocatalytic process. Research on the catalytic applications of type III heterojunctions remains limited. Unlocking the potential of type III heterojunctions requires suitable conductive media to overcome the high energy barriers that inhibit charge transfer.[53] Effective pairing of photogenerated

holes in the VB of semiconductor B with photogenerated electrons in the CB of semiconductor A could significantly enhance their photocatalytic and photothermal catalytic performance. Moreover, the design of type III heterojunctions should consider the alignment of energy levels not only at the interface but also the overall electronic structure of the materials involved, as this can influence the efficiency of charge separation and transfer.

3.2 Schottky heterojunction

A Schottky heterojunction forms between a semiconductor and a metal with different Fermi levels (Fig. 2d), producing a Schottky barrier in semiconductor–metal nanocomposites.[56,57] The work function difference drives charge exchange at the interface.[58] This charge exchange is crucial as it establishes an electric field at the junction, which influences the movement of charge carriers. In an n-type semiconductor–metal Schottky heterojunction, electrons flow from the semiconductor to the metal upon contact until their Fermi levels equilibrate.[59] This process not only results in the formation of a positively charged region in the semiconductor but also alters the energy band structure significantly. Due to the limited density of free electrons, a positively charged region forms in the semiconductor, causing its energy bands to bend upward and creating a Schottky barrier at the metal–semiconductor interface. The height of this Schottky barrier is determined by the difference in work function between the metal and the semiconductor, which plays a critical role in dictating the efficiency of charge carrier separation and transport. The movement of carriers across the Schottky heterojunction is driven by the Fermi level difference between the semiconductor and the metal.[60] Under illumination, photogenerated holes in the semiconductor are driven by the internal electric field (IEF) toward the metal, where it acts as a hole trap and an active site for photo-oxidation, enhancing charge carrier separation. This trapping mechanism is essential as it prevents the recombination of photogenerated holes and electrons, thereby increasing the availability of reactive holes for oxidation reactions. The efficiency of this process is influenced by factors such as the thickness of the Schottky barrier and the interface quality, which can affect the rate of charge transfer. The Schottky barrier prevents photogenerated electron migration to the metal.[61] This structure promotes continuous migration of photogenerated electrons under light excitation, enhancing photogenerated charge separation, facilitating hole participation, and improving photocatalytic performance.[62]

3.3 Z-scheme heterojunctions

Despite the excellent electron–hole separation efficiency of the aforementioned heterojunctions, their overall redox capability remains limited because oxidation and reduction occur on semiconductors with relatively low oxidation and reduction potentials, respectively. This limitation arises from the intrinsic bandgap energies of the semiconductors used, which dictate their ability to participate in redox reactions. The energy levels of the conduction band (CB) and valence band (VB) must be appropriately aligned with the redox potentials of the target reactions to achieve effective charge transfer. The "Z-scheme"

photocatalytic system is a type of photocatalytic mechanism that mimics natural photosynthesis, where two semiconductors are coupled to facilitate the separation and transfer of photogenerated charge carriers. In this system, one semiconductor acts as an electron donor while the other serves as an electron acceptor, allowing for efficient charge separation and redox reactions. To address these limitations, Bard et al. proposed constructing a traditional Z-scheme photocatalytic system (also known as a liquid-phase heterojunction).[63] Inspired by the electron transfer pathways in natural photosynthetic systems,[64] the ideal charge transfer mechanism achieves efficient photogenerated charge carrier separation while maintaining efficient redox capability.[65] However, forming liquid-phase Z-scheme heterojunctions is constrained by the need to couple specific electron acceptor/donor (A/D) pairs, as illustrated in Fig. 2e.[66] The selection of these A/D pairs is critical, as it directly influences the thermodynamic feasibility of the redox reactions. The alignment of the energy levels of the acceptors and donors with the band positions of the photocatalysts determines the efficiency of charge transfer and the overall photocatalytic performance. CB electrons from PC II, with a lower band position, are captured by acceptor A and reduced to donor D.[67] Similarly, VB holes in PC I are captured by donor D and oxidized to acceptor A, completing the cycle.[68] Due to the higher electron potential in PC I, its electrons more readily participate in the reduction reaction of A, while holes in PC II more easily participate in the oxidation reaction of D.[69] The traditional Z-scheme photocatalytic system is becoming less favored due to its complex structure, high uncertainty, and limited applicability. To provide a more comprehensive understanding of the photogenerated carrier dynamics in Z-type and S-type heterojunctions, we have included an analysis of the carrier migration pathways and their interactions with the semiconductor interfaces. These challenges include difficulties in optimizing the interface between the semiconductor and the liquid phase, which can lead to mass transfer limitations and reduced reaction rates. In Z-type heterojunctions, the spatial separation of charge carriers is crucial for enhancing photocatalytic efficiency. The dynamics of photogenerated carriers involve their migration from the conduction band of one semiconductor to the valence band of another, facilitated by the energy level alignment. This process is influenced by factors such as the thickness of the semiconductor layers and the presence of defects that can trap carriers, thus affecting their mobility. To improve charge transfer and broaden applications, Tada et al. proposed the all-solid-state Z-scheme photocatalytic system in 2006.[70] This system uses two distinct semiconductors and a metal conductor as an electron mediator.[71] The introduction of a metal conductor not only facilitates electron transfer but also helps to stabilize the charge carriers, reducing the likelihood of recombination. In this configuration, the dynamics of charge carriers are enhanced by the rapid electron transfer through the metal conductor, which minimizes the distance that electrons must migrate, thereby reducing recombination losses. This configuration allows for a more efficient spatial separation of charge carriers compared to traditional liquid-phase systems. This heterojunction overcomes the limitation of traditional

liquid-phase Z-scheme systems by shortening electron migration distance which could enhance photocatalytic performance.[72] As shown in Fig. 2f, the all-solid-state Z-scheme photocatalyst consists of two semiconductors and an electron mediator.[73] Under illumination, electrons in the VB of semiconductor II are excited to the CB and transferred through the electron mediator to the VB of semiconductor I, where they recombine with holes.[74] This process is driven by the internal electric field established at the junctions, which promotes the directional flow of charge carriers. The dynamics of this charge transfer are further influenced by the band alignment between the semiconductors, which dictates the energy barriers for carrier migration. A favourable alignment can enhance the efficiency of charge separation and reduce the likelihood of recombination. The efficiency of this charge transfer is influenced by factors such as the band alignment between the semiconductors and the properties of the electron mediator. The remaining reducing electrons in PC II and oxidizing holes in PC I participate in reduction and oxidation reactions, achieving spatial separation of electrons and holes and high redox potentials.[75] However, in practice, photogenerated carriers with strong redox capabilities tend to associate with specific electron acceptor/donor pairs in liquid-phase Z-scheme heterojunctions or with metal conductors in all-solid-state Z-scheme heterojunctions. This association can lead to limitations in the versatility of the photocatalytic systems, as the choice of materials and their compatibility with the desired redox reactions are crucial for optimizing performance. A deeper understanding of the carrier dynamics, including the rates of charge transfer and the effects of various environmental conditions, is essential for advancing the design of more efficient photocatalysts.

3.4 S-scheme heterojunction

In 2019, Yu and colleagues reported the S-type heterojunction,[76] which improves redox capabilities while maintaining high activity, clarifying carrier transfer mechanisms in photocatalytic reactions. The S-type heterojunction represents a significant advancement in photocatalytic design, as it effectively utilizes the distinct redox potentials of two semiconductors to enhance overall photocatalytic efficiency. As illustrated in Fig. 2g, the S-type heterojunction consists of two semiconductors: an oxidative photocatalyst (OP) and a reductive photocatalyst (RP). RP has a more negative CB position and smaller work function than OP.[77] As shown in Fig. 2h, due to its higher Fermi level, electrons in RP transfer spontaneously to OP upon contact, which results in a positive charge on RP and causes its energy bands to bend upward.[50,78] This upward bending of energy bands in RP indicates a depletion of electrons, which is critical for establishing a driving force for electron transfer. The energy band alignment between RP and OP is crucial, as it dictates the efficiency of charge separation and the subsequent redox reactions. When the Fermi level equilibrium is reached between RP and OP, the interface near OP becomes negatively charged due to electron acquisition, causing its energy bands to bend downward.[79] Consequently, an IEF forms at the interface, directed from RP to OP.[80] To provide a more comprehensive

understanding of the photogenerated carrier dynamics in S-type heterojunctions, we have included an analysis of the carrier migration pathways and their interactions with the semiconductor interfaces. Under illumination, as depicted in Fig. 2i, the IEF and Coulombic interactions cause electrons in the CB of OP and holes in the VB of RP to recombine at the contact interface, promoting carrier separation and eliminating non-useful charge carriers.[81] This recombination process is essential for enhancing the photocatalytic activity, as it ensures that the photogenerated carriers are effectively utilized in redox reactions rather than recombining and losing their energy. The dynamics of these carriers involve their movement through the semiconductor layers, influenced by the band structure and the established IEF. The efficiency of this process is contingent upon the alignment of energy levels and the distance over which carriers must migrate. Photogenerated carriers with stronger redox capabilities are retained for photocatalytic reactions.[82] Coulombic repulsion and the IEF direction prevent electron transfer from the CB of RP to that of OP, suppressing undesirable electron transfer and reverse reactions.[83] This mechanism of charge separation is particularly advantageous because it minimizes the chances of recombination losses, which are often a significant limitation in traditional photocatalytic systems. The strategic design of the S-type heterojunction thus allows for enhanced charge carrier dynamics, leading to improved photocatalytic performance. Thus, the S-scheme heterojunction facilitates the separation and transfer of light-induced carriers while maintaining robust redox capabilities. By leveraging the unique properties of both OP and RP, the S-type heterojunction not only enhances the efficiency of charge separation but also optimizes the redox potential for various photocatalytic applications, making it a promising approach for future photocatalyst development. Understanding these physicochemical principles is essential for further advancements in the field of photocatalysis.

4. Applications of BiVO$_4$-based heterojunction photocatalysts

Semiconductor photocatalytic technology has significant promise for energy conversion and environmental remediation by efficiently transforming solar energy into chemical energy.[84,85] Sunlight-driven photocatalytic reactions occur under mild conditions, making them well-suited for green and sustainable development.[86] However, traditional semiconductor materials have limited photocatalytic performance due to their low energy conversion efficiency and poor visible light responsiveness, restricting their practical applications. Recently, BiVO$_4$-based heterojunction photocatalysts have emerged as a research focus due to their superior performance.[87,88] As shown in Fig. 3, photogenerated electrons and holes migrate to the surface of the photocatalyst, driving surface reduction and oxidation reactions, respectively. These catalysts have achieved significant advancements in photocatalytic water splitting, nitrogen cycling, CO$_2$ reduction, pollutant degradation, HCHO removal, and bacterial inactivation. By rationally designing heterojunction structures,
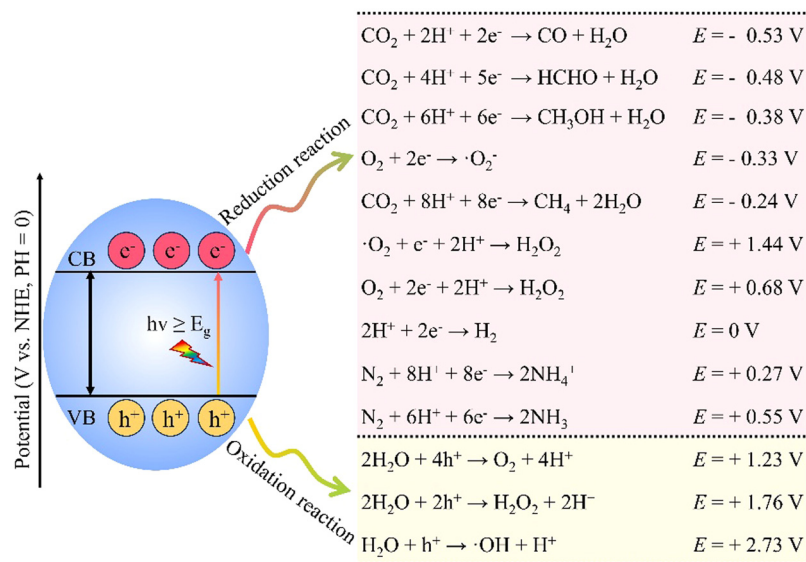
$$CO_2 + 2H^+ + 2e^- \rightarrow CO + H_2O \qquad E = -0.53 \text{ V}$$
$$CO_2 + 4H^+ + 5e^- \rightarrow HCHO + H_2O \qquad E = -0.48 \text{ V}$$
$$CO_2 + 6H^+ + 6e^- \rightarrow CH_3OH + H_2O \qquad E = -0.38 \text{ V}$$
$$O_2 + 2e^- \rightarrow \cdot O_2^- \qquad E = -0.33 \text{ V}$$
$$CO_2 + 8H^+ + 8e^- \rightarrow CH_4 + 2H_2O \qquad E = -0.24 \text{ V}$$
$$\cdot O_2^- + e^- + 2H^+ \rightarrow H_2O_2 \qquad E = +1.44 \text{ V}$$
$$O_2 + 2e^- + 2H^+ \rightarrow H_2O_2 \qquad E = +0.68 \text{ V}$$
$$2H^+ + 2e^- \rightarrow H_2 \qquad E = 0 \text{ V}$$
$$N_2 + 8H^+ + 8e^- \rightarrow 2NH_4^+ \qquad E = +0.27 \text{ V}$$
$$N_2 + 6H^+ + 6e^- \rightarrow 2NH_3 \qquad E = +0.55 \text{ V}$$
$$2H_2O + 4h^+ \rightarrow O_2 + 4H^+ \qquad E = +1.23 \text{ V}$$
$$2H_2O + 2h^+ \rightarrow H_2O_2 + 2H^- \qquad E = +1.76 \text{ V}$$
$$H_2O + h^+ \rightarrow \cdot OH + H^+ \qquad E = +2.73 \text{ V}$$

Fig. 3 Schematic illustration of the photocatalytic processes (hv: illumination; E_g: bandgap).

the separation and transport efficiency of photogenerated charges can be significantly enhanced, improving photocatalytic activity and endowing $BiVO_4$-based catalysts a competitive advantage edge in photocatalytic technology. This section will provide an overview of $BiVO_4$-based heterojunctions in photocatalytic applications, highlighting their advancements in energy conversion and environmental remediation, and their critical role in addressing challenges in photocatalytic technologies.

4.1 Energy conversion applications

$BiVO_4$-based heterojunctions exhibit remarkable multifunctionality in photocatalytic energy conversion applications, including water splitting,[89] nitrogen fixation,[90] CO_2 reduction,[91] and hydrogen peroxide (H_2O_2) synthesis.[92] These capabilities highlight their significance in advancing energy conversion technologies. By harnessing solar energy, these materials are crucial for sustainable energy production and environmental remediation, addressing global energy and environmental challenges.

4.1.1 Water splitting. As global energy demand rises, utilizing solar energy for water splitting to produce clean hydrogen presents a significant challenge in chemistry.[93] $BiVO_4$ has gained attention for its unique optical and electronic properties,[94] including a narrow E_g and a VB position suitable for water oxidation, with its CB close to the hydrogen evolution potential.[95] However, practical applications of $BiVO_4$ are hindered by high carrier recombination rates and low kinetics for oxygen evolution, limiting its solar-to-chemical energy conversion efficiency. To address these issues, researchers have explored various heterojunction designs. A comparative analysis of existing literature reveals differing perspectives on the stability and performance of $BiVO_4$-based heterojunctions. For instance, while Chaudhary *et al.* demonstrated that embedding SnS_2 nanoparticles in $BiVO_4$ films resulted in a 2.73-fold increase in photocurrent density, they noted that the stability of the heterojunction

under prolonged illumination remains a concern (Fig. 4a–f).[96] In contrast, Sánchez-Albores *et al.* reported that their $BiVO_4$/$ZnFe_2O_4$ heterojunction showed promising light absorption and charge transfer capabilities; however, they highlighted that increased deposition thickness led to particle aggregation, adversely affecting photocatalytic activity.[97] This suggests that while enhancing charge separation is crucial, maintaining structural integrity and stability is equally important for practical applications.

Our research team has introduced a novel strategy to overcome these limitations by achieving constrained growth of Co–Pi co-catalysts on $BiVO_4$ using a polydopamine matrix (Fig. 4g).[98] This approach enhances co-catalyst anchoring and dispersion while facilitating effective organic–inorganic interactions, resulting in a photocurrent density of 2.47 mA cm^{-2} (1.23 V *vs.* RHE), approximately 7 times higher than that of bare $BiVO_4$ (Fig. 4h). Additionally, the charge injection efficiency improved from 25% to 75% (Fig. 4i), achieving a 27% incident photon-to-current efficiency (IPCE) at 400 nm (Fig. 4j). In comparison to previous studies, our method not only focuses on surface passivation and interface enhancement but also promotes the ordered growth of Co–Pi, which is critical for improving charge separation and stability. This dual approach offers new insights for efficient photocatalytic water splitting, addressing both performance and longevity concerns that have been raised in the literature (Fig. 4k). A summary of the water-splitting performance of $BiVO_4$-based heterojunction photocatalysts is presented in Table 1.[99–114]

4.1.2 Nitrogen fixation. Ammonia (NH_3) is essential for industrial and agricultural applications, serving as a key component in chemical transformations and an efficient medium for energy storage and transmission.[115] Green NH_3 is increasingly recognized as an optimal choice for sustainable fuel and hydrogen carriers, supporting the transition to an "NH_3 economy."[116] However, the traditional Haber–Bosch process is energy-
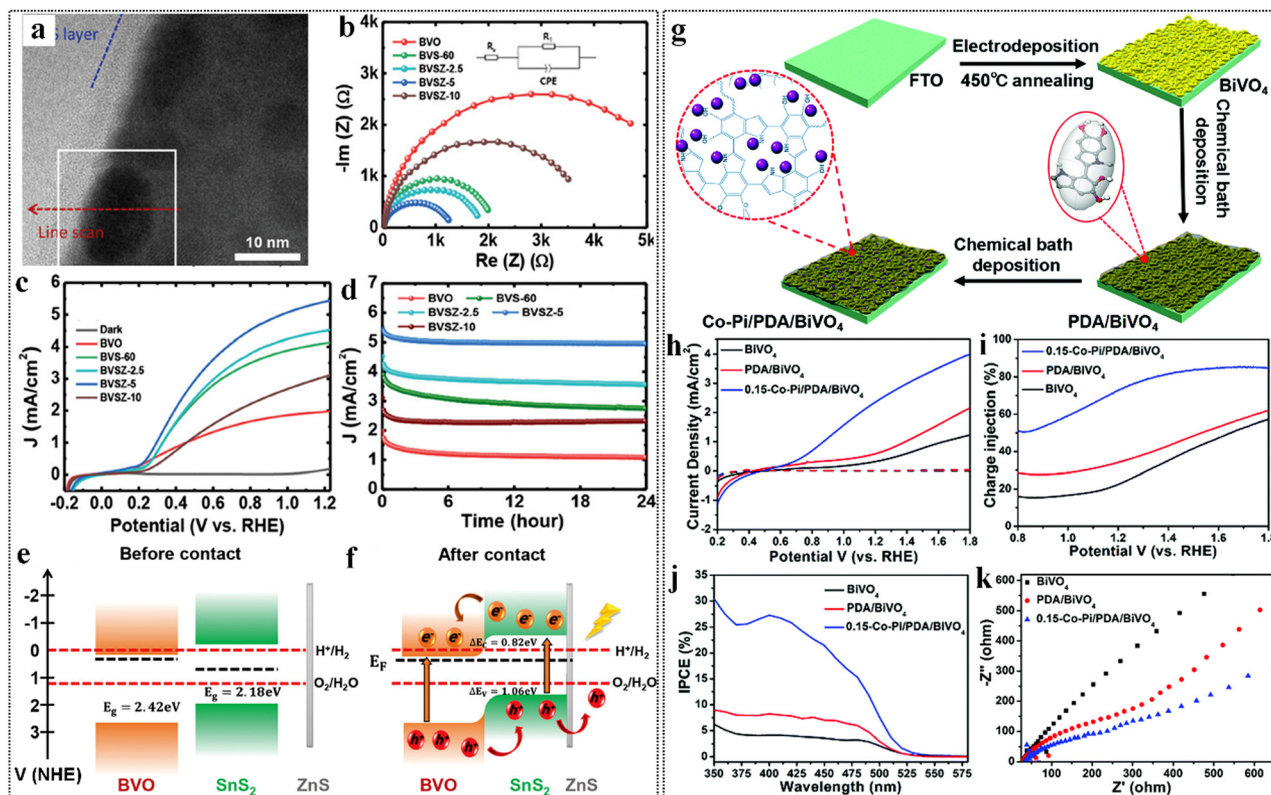
Fig. 4 (a) A BFTEM cross-sectional image for a $BiVO_4$ film with embedded SnS_2 nanoparticles and a ZnS coating layer. (b) EIS Nyquist plots, (c) LSV curves, and (d) stability curves for the BVO, BVS-60, BVSZ-2.5, BVSZ-5, and BVSZ-10 photoanodes. (e) and (f) Band diagrams of a $BVO/SnS_2/ZnS$ photoanode before and after contact. Reproduced from ref. 96 with permission from Wiley, copyright 2024. (g) Synthesis of $Co–Pi/PDA/BiVO_4$. (h) $J–V$ plots of $BiVO_4$, $PDA/BiVO_4$, and $0.15-Co–Pi/PDA/BiVO_4$. (i) Charge injection efficiencies. (j) IPCE spectra. (k) PEIS plots of $BiVO_4$, $PDA/BiVO_4$, and $0.15-Co–Pi/PDA/BiVO_4$. Reproduced from ref. 98 with permission from Royal Society of Chemistry, copyright 2019.

Table 1 Comparison of the water-splitting performance of the reported $BiVO_4$-based heterojunction photocatalysts

Photoelectrode design	Light source (W Xe-lamp)	Electrolyte used	ABPE (%)	IPCE	Photocurrent density (mA cm^{-2}) (1.23 V$_{RHE}$)	Ref.
$BiVO_4/ZnIn_2S_4$	300	0.2 M Na_2SO_4	—	—	0.42	99
$BiVO_4/C_3N_4$	300	0.5 M KBi	2.48	85% at 380–460 nm	5.89	100
$CuMTZ/BiVO_4$	300	1 M KPi	1.04	92.5% at 400 nm	3.32	101
$BiVO_4/BiOBr$	300	0.5 M Na_2SO_4	0.26	51% at 340 nm	2.69	102
$MW:BiVO_4@CFO/TANF$	300	0.1 M Na_2SO_4	1.35	45.9% at 380 nm	6.03	103
OVs $BiVO_4/Bi_2MoO_6$	300	0.5 M Na_2SO_4	0.12	—	0.34	104
$CdSe/BiVO_4$	300	0.5 M Na_2SO_4	—	—	0.155	105
$BiVO_4/CuBi_2O_4$	300	0.2 M PBS	—	12% at 350–500 nm	1.15	106
$N-WO_3/BiVO_4$	500	0.5 M Na_2SO_4	—	—	0.78	107
$NiMoO_4/BiVO_4/Sn:WO_3$	150	1 M KPi	0.52	38.3% at 450 nm	2.06	108
$g-C_3N_4/ThO_2@BiVO_4$	300	0.5 M Na_2SO_4	0.44	—	0.45	109
$BVO/BiVO_4$	300	0.5 M KBi	2.0	60% at 470 nm	3.40	110
$N-CFO/BiVO_4$	300	0.1 M KBi	—	87% at 370 nm	4.83	111
$CNODs/BiVO_4$ ODs	300	0.05 M Na_2SO_4	0.24	—	2.2	112
$BiVO_4/In_2O_3/FeNi$	300	0.5 M Na_2SO_4	0.95	—	4.00	113
$BiVO_4–Co-MOF$	300	0.5 M Na_2SO_4	—	—	2.32	114

intensive and environmentally detrimental, highlighting the need for eco-friendly NH_3 synthesis methods under ambient conditions.[117] Photocatalytic NH_3 synthesis offers an ideal, sustainable, and energy-efficient solution.[118] Since Schrauzer and Guth's initial report on TiO_2-based photocatalysts for nitrogen fixation in 1977, this field has become a leading focus

of photocatalytic research.[14] Heterojunction photocatalysts, combining various semiconductor materials, enhance performance through synergistic effects.[119] Among these, $BiVO_4$-based heterojunctions stand out for their superior optical properties and favorable band structure,[90] making them critical in advancing nitrogen fixation technologies.

A comparative analysis of existing literature reveals varying conclusions regarding the stability and efficiency of $BiVO_4$-based heterojunctions. For instance, Chen *et al.* fabricated a $BiVO_4$ photoanode with an MgO interlayer, achieving significant improvements in photocurrent density and PEC conversion efficiency (Fig. 5a and b).[120] However, they noted that while the MgO interlayer reduced surface defects, the long-term stability of the heterojunction under operational conditions remains a concern (Fig. 5c–f). In contrast, our group's investigation into the CoFeMnO/$BiVO_4$ heterojunction demonstrated a signal recovery time of 9.1 picoseconds, indicating enhanced electron dynamics and stability during photocatalytic reactions (Fig. 5g and h).[121] This suggests that while various strategies can improve performance, the stability of the heterojunctions under continuous operation is crucial for practical applications.

In comparing our findings with those of other research teams, it is evident that the introduction of structural modifications, such as the incorporation of FLPs, significantly enhances catalytic performance and selectivity (Fig. 5i–k).[122] While some studies have focused on optimizing the electronic properties of $BiVO_4$-based heterojunctions, our research highlights the importance of both structural and electronic enhancements to achieve superior stability and efficiency in NH_3 synthesis. We validated the NH_3 evolution process using isotopic ^1H nuclear magnetic resonance spectroscopy with $^{15}NO_3^-$ as the nitrogen source, ensuring the reliability of our results (Fig. 5l).

This research elucidates the critical role of FLPs in enhancing selective chemical adsorption and catalytic kinetics, broadening the application prospects of FLP active sites in PEC-NITRR. The nitrogen fixation performance of $BiVO_4$-based heterojunction photocatalysts are listed in Table 2.[90,120,123–133]

4.1.3 CO_2 reduction. The international energy agency (IEA) reports that global energy-related CO_2 emissions reached 37.4 billion tons in 2023, reflecting a 1.1% increase from the previous year. Consequently, there is an urgent need to transform CO_2 utilization, prompting investors to focus on technologies that convert CO_2 into valuable chemicals. The significance of carbon capture facilities has intensified amid ongoing fossil fuel reliance. Large-scale CO_2 capture and the production of high-energy chemicals are crucial for reversing combustion processes used in transport fuel production.[134] Photocatalytic CO_2 reduction emerges as a promising alternative, offering substantial environmental and economic benefits. Although costs under UV light remain high, recent research has shifted toward utilizing visible light (solar energy), a free and abundant resource that necessitates advanced photocatalyst development.

A comparative analysis of existing literature highlights varying approaches and conclusions regarding the stability and efficiency of $BiVO_4$-based heterojunctions. For instance, Ahmadi *et al.* synthesized $BiVO_4$/TiO_2 photocatalysts with varying molar ratios (1:1, 1:2, 1:3, and 1:4) to evaluate their performance in CO_2 reduction.[135] Their findings indicated that
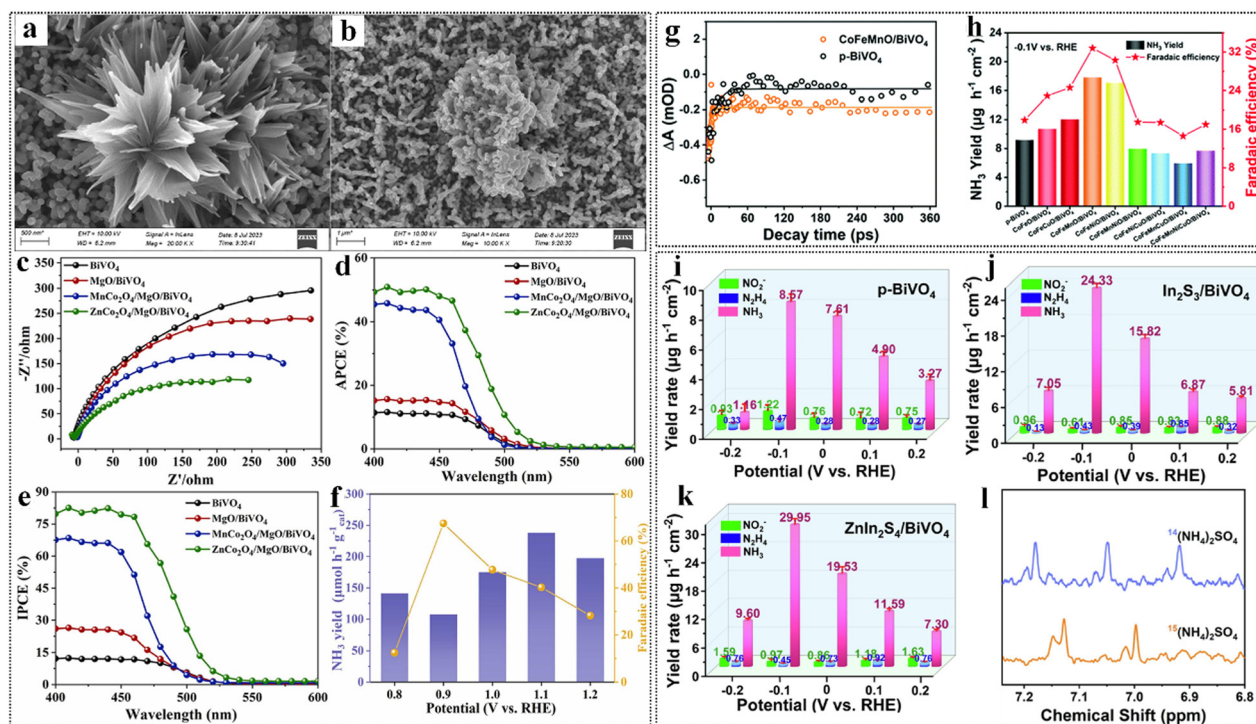
Fig. 5 (a) SEM images of $MnCo_2O_4$/MgO/$BiVO_4$ and (b) $ZnCo_2O_4$/MgO/$BiVO_4$. (c) EIS, (d) APCE and (e) IPCE diagrams of $BiVO_4$, MgO/$BiVO_4$, MCo_2O_4/$BiVO_4$ (M = Zn, Mn) and MCo_2O_4/MgO/$BiVO_4$ (M = Zn, Mn). (f) Ammonia formation rates (the average value on 2 h reaction) and corresponding faradaic efficiencies of $ZnCo_2O_4$/MgO/$BiVO_4$. Reproduced from ref. 120 with permission from Elsevier, copyright 2024. (g) Characteristic dynamics of p-$BiVO_4$ and CoFeMnO/$BiVO_4$ probed at 480 nm. (h) Yield of NH_3 and faradaic efficiency (A-M_XO_Y/p-$BiVO_4$) at −0.1 V *vs.* RHE. Reproduced from ref. 121 with permission from Royal Society of Chemistry, copyright 2022. Yield rates of (i) p-$BiVO_4$, (j) In_2S_3/$BiVO_4$ and (k) $ZnIn_2S_4$/$BiVO_4$ under different voltages. (l) Qualitative experiments of $^{14}NO_3^-$ and $^{15}NO_3^-$ isotopes. Reproduced from ref. 122 with permission from Elsevier, copyright 2022.

Table 2 Summary of the photocatalytic nitrogen fixation activity of $BiVO_4$-based heterojunction photocatalysts

Photoelectrode design	Source of N	Light source (W Xe-lamp)	NH_3 yield	Testing method	Ref.
$Cs_3Mo_xSb_yBr_9/BiVO_4$	N_2	300	$300 \pm 5\ \mu mol\ h^{-1}\ g^{-1}$	Indophenol blue method	123
$Bi/BiVO_4$	N_2	300	$167.74\ \mu mol\ h^{-1}\ g^{-1}$	Nessler's reagent	124
$BiVO_4/CuPc$	NO_3^-	300	$12.98\ \mu g\ h^{-1}\ cm^{-2}$	Nessler's reagent	125
Coupling $BiVO_4$–RuO_2 with PPV–Cu	NO_3^-	300	—	Indophenol blue method	126
CeO_2–$C/BiVO_4$	NO_3^-	300	$21.81\ \mu g\ h^{-1}\ cm^{-2}$	Nessler's reagent	127
$Fe^{2+}Cu^{2+}Fe^{3+}LDH/BiVO_4$	NO_3^-	300	$13.8\ \mu g\ h^{-1}\ cm^{-2}$	Nessler's reagent	128
$Ru/BiVO_4$–V_O	N_2	300	$3.88\ \mu mol\ h^{-1}\ g^{-1}$	Nessler's reagent	129
$ZnCo_2O_4/MgO/BiVO_4$	N_2	300	$35.52\ \mu mol\ h^{-1}\ g^{-1}$	Indophenol blue method	120
$BiVO_4/V_S$–MoS_2	N_2	300	$132.8\ mmol\ h^{-1}\ g^{-1}$	Indophenol blue method	90
V_O–BP–$BiVO_4$	N_2	300	$208\ \mu mol\ h^{-1}\ g^{-1}$	Nessler's reagent	130
$Co_3O_4/BiVO_4$	N_2	300	$35\ \mu mol\ h^{-1}\ g^{-1}$	Nessler's reagent	131
$BiVO_4@MXene$	N_2	300	$27.25\ \mu g\ h^{-1}\ cm^{-2}$	Indophenol blue method	132
$BiVO_4/V_S/ZnIn_2S_4$	N_2	300	$80.6\ \mu mol\ h^{-1}\ g^{-1}$	Nessler's reagent	133
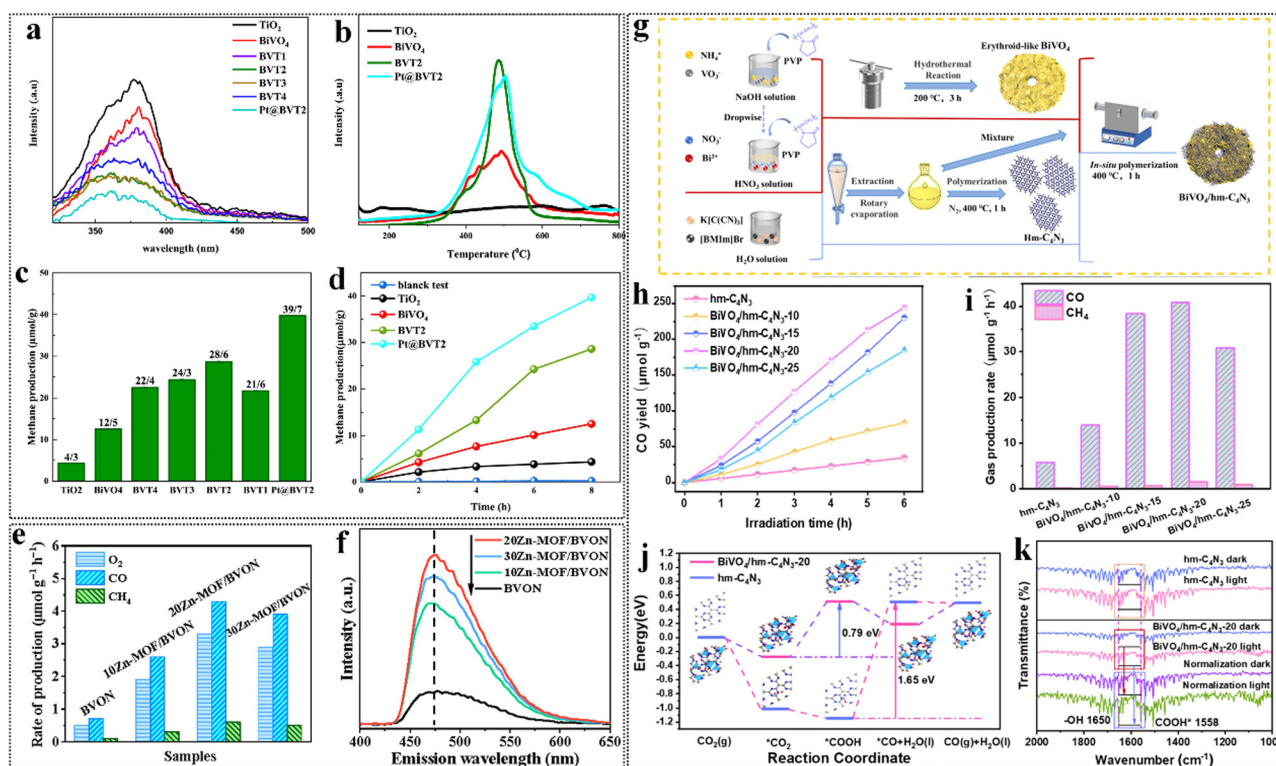
Fig. 6 (a) Photoluminescence spectra of the synthesized photocatalysts. (b) CO_2-TPD results of TiO_2, $BiVO_6$, $BVT2$ and $Pt@BVT2$ from 30 to 800 °C. (c) CH_4 yield over different photo-catalysts after 8 h of reaction. (d) CH_4 yield over different photo-catalysts during 8 h of reaction. Reproduced from ref. 135 with permission from Elsevier, copyright 2024. (e) Photocatalytic activities for CO_2 conversion of BVON and xZn-MOF/BVON heterojunctions under visible-light irradiation. (f) FS related to the formed ·OH amount. Reproduced from ref. 136 with permission from Elsevier, copyright 2022. (g) Illustration for the preparation of erythroid-like $BiVO_4/hm$-C_4N_3 hybrids. (h) and (i) Time evolutions of CO and average gas production rates over different catalysts. (j) The free energy diagrams of CO_2 reduction to CO for hm-C_4N_3 (blue line) and $BiVO_4/hm$-C_4N_3 composite (red line) based on DFT calculation. (k) In situ DRIFTS spectra of CO_2 photoconversion over different samples. Reproduced from ref. 137 with permission from Elsevier, copyright 2021.

the heterojunction structure significantly improved optical performance and electron–hole separation efficiency (Fig. 6a–d). However, while the BVT_2 sample achieved the highest methane yield, the long-term stability of these photocatalysts under continuous operation was not thoroughly addressed. In contrast, Zhao et al. developed an S-type heterojunction (Zn-MOF/BVON) that exhibited a 22-fold increase in light activity compared to previously reported $BiVO_4$ nanosheets.[136] This enhancement was attributed to improved charge transfer and separation, but the

authors also emphasized the importance of stability in practical applications, suggesting that the size-matched Zn-MOF/BVON structure not only facilitates efficient charge separation but also provides abundant catalytic active sites, which may contribute to enhanced stability over time (Fig. 6e and f).

Wu et al. developed a layered, red blood cell-like $BiVO_4/hm$-C_4N_3 direct Z-type heterojunction using template induction and in situ polymerization (Fig. 6g).[137] This Z-type system effectively integrates CO_2 capture, activation, and charge transfer,

resulting in outstanding catalytic performance. It converts CO_2 and H_2O into CO and O_2 without requiring sacrificial agents or co-catalysts. The optimized $BiVO_4$/hm-C_4N_3 catalyst achieved a CO generation rate of up to 40.8 μmol g^{-1} h^{-1} with over 97% selectivity (Fig. 6a and i). In comparing these studies, it is evident that while different strategies have been employed to enhance photocatalytic performance, the stability of the $BiVO_4$-based heterojunctions remains a critical factor for their practical application. For example, the DFT calculations and *in situ* diffuse reflectance infrared Fourier transform spectroscopy

(DRIFTS) analyses conducted by Wu *et al.* revealed that $BiVO_4$ facilitates proton replenishment through H_2O oxidation, which may contribute to the stability of the photocatalytic process (Fig. 6j and k). This indicates that understanding the underlying mechanisms that enhance both performance and stability is essential for advancing the field of photocatalytic CO_2 reduction. This research presents an innovative strategy for developing organic semiconductor-based photocatalysts, paving the way for advancements in artificial photosynthesis. A comparison of CO_2 reduction performances

Table 3 Summary of the photocatalytic CO_2 reduction performance of reported $BiVO_4$-based heterojunction photocatalysts

Photoelectrode design	Mass of sample	Light source	Reduction products	Testing time (h)	Yield	Ref.
tBi_2S_3/$BiVO_4$–E	30 mg	300 W Xe-lamp	CH_3OH	10	290.45 μmol g^{-1} h^{-1}	138
Fe_3O_4/$BiVO_4$	20 mg	20 W LED light (λ = 415 nm)	CH_3OH	12	371 mmol g^{-1}	139
CuTcPc/$BiVO_4$	20 mg	300 W Xe-lamp	CO	3	42 μmol g^{-1} h^{-1}	140
$BiVO_4$|Au|Eu_2Ti_4	Film catalyst	300 W Xe-lamp ($\lambda \leq$ 500 nm)	CO	5	0.38 μmol m^{-2} h^{-1}	141
$BiVO_4$@PCN-224(Cu)	10 mg	300 W Xe-lamp	CO	1	70.5 μmol g^{-1} h^{-1}	142
Au–$BiVO_4$/P-CN	5 mg	300 W Xe-lamp	CO	1	20.87 μmol g^{-1} h^{-1}	143
BiOBr/$BiVO_4$	Film catalyst	300 W Xe-lamp	CO	6	95.27 mmol g^{-1} h^{-1}	144
$BiVO_4$/TiO_2	0.1 g	UV Hg 8 W pen-ray lamp	CO	7	1.6 μmol g$_{cat}$$^{-1}$	135
Pt@$BiVO_4$/2TiO_2	100 mg	250 W mercury vapor lamp	CH_4	8	39.7 μmol g^{-1}	145
Cu_1–TiO_2/$BiVO_4$-4	30 mg	300 W Xe-lamp	CO	1	17.33 μmol g$_{cat}$$^{-1}$ h^{-1}	146
$CsPbBr_3$/$BiVO_4$	8 mg	300 W Xe-lamp	CO	4	41.02 μmol g^{-1} h^{-1}	147
$BiVO_4$/$Bi_{19}Cl_3S_{27}$	15 mg	300 W Xe-lamp	CO	4	80.94 μmol g^{-1}	148
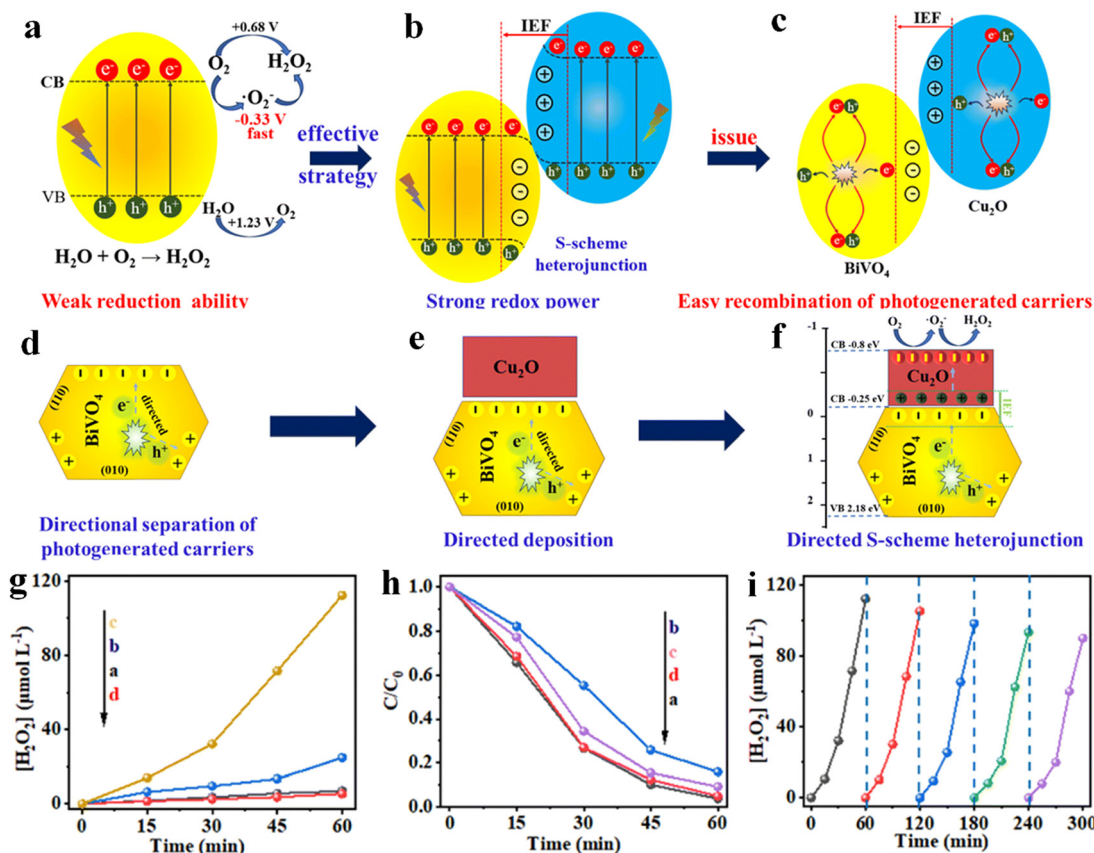
Fig. 7 (a)–(f) Graphical illustration showing the design of the S-scheme heterojunction for highly active H_2O_2 production. (g) Photocatalytic H_2O_2 production and (h) time-dependent curves of photocatalytic H_2O_2 decomposition of various samples. (i) Cycle test for the MnOOH/$BiVO_4$/Cu_2O photocatalyst. Reproduced from ref. 149 with permission from Royal Society of Chemistry, copyright 2024.

of BiVO$_4$-based heterojunction photocatalysts is presented in Table 3.[135,138–148]

4.1.4 H$_2$O$_2$ synthesis. H$_2$O$_2$ is widely used in wastewater treatment and fuel cells, yet traditional synthesis methods are costly and complex. Photocatalytic technology offers a low-cost and sustainable alternative for large-scale H$_2$O$_2$ production. However, challenges such as rapid recombination of photo-generated electrons and holes and slow reaction kinetics hinder efficiency. Constructing S-type heterojunctions can significantly enhance charge carrier separation and redox capabilities. A comparative analysis of existing literature reveals diverse approaches and conclusions regarding the stability and efficiency of BiVO$_4$-based heterojunctions. For instance, Huang *et al.* synthesized a MnOOH co-catalyst-modified BiVO$_4$/Cu$_2$O

S-type heterojunction, which created dual electric fields that improve charge separation (Fig. 7a–f).[149] Their findings demonstrated that in pure water, this heterojunction exhibited a H$_2$O$_2$ generation capacity of 112 μmol L^{-1}, approximately 16 times that of pure BiVO$_4$ (Fig. 7g–i). However, while this study highlights the enhanced performance of the S-type heterojunction, it does not extensively address the long-term stability of the BiVO$_4$ component under operational conditions.

This study demonstrates the potential of S-type heterojunctions for efficient H$_2$O$_2$ synthesis and large-scale production.

4.2 Environmental remediation applications

BiVO$_4$-based heterojunctions exhibit significant versatility in photocatalytic environmental remediation applications,
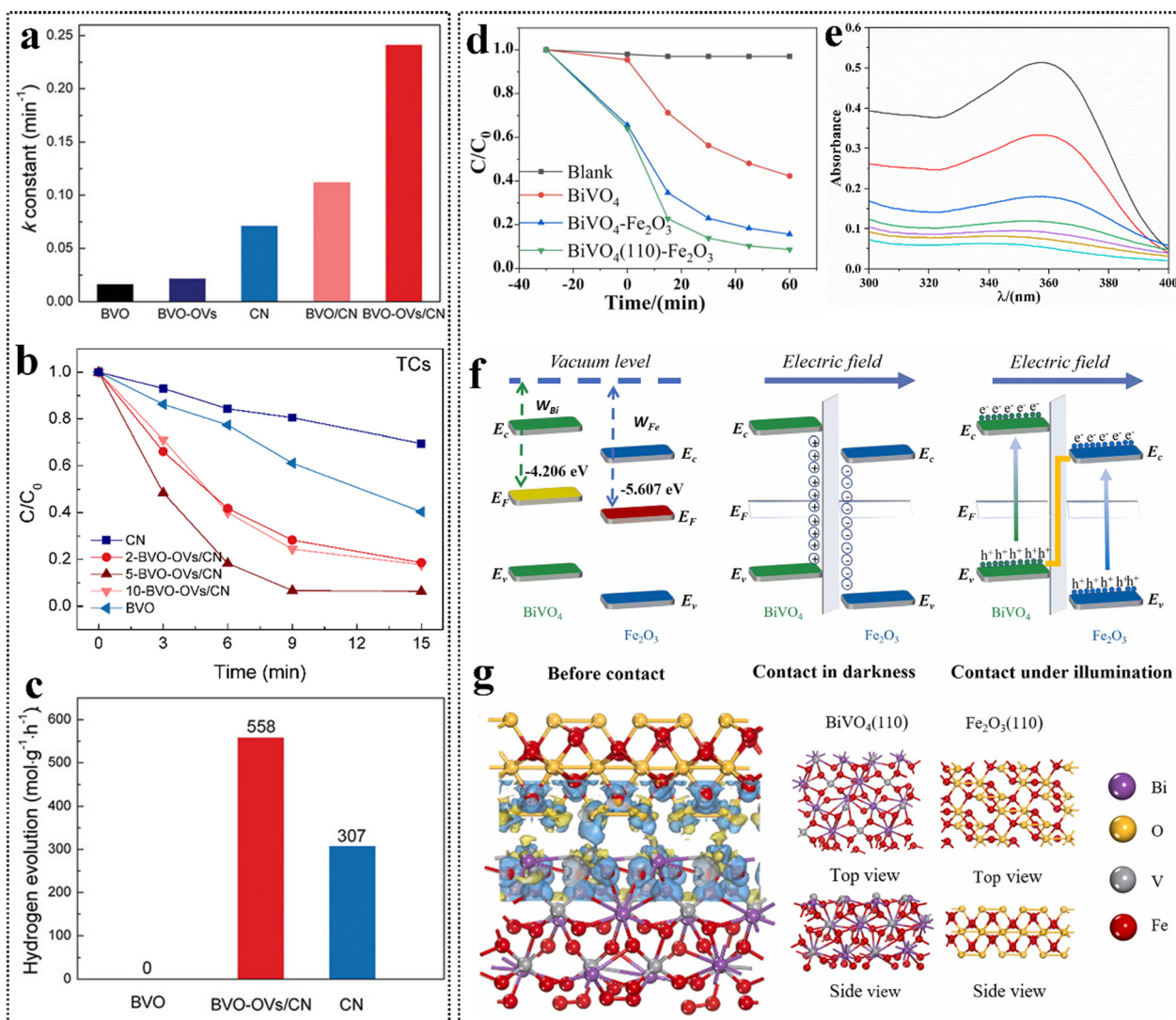
Fig. 8 (a) Corresponding first-order kinetic k constant of BVO, BVO-OVs, CN, BVO/CN, and BVO-OVs/CN. (b) Photodegradation on TC pollutant of BVO, CN and BVO-OVs/CN with different BVO-OVs and CN ratios. (c) Comparison of photocatalytic hydrogen evolution rate. Reproduced from ref. 155 with permission from Wiley, copyright 2024. (d) Photocatalytic degradation of tetracycline by different samples. (e) Curve of absorbance with tetracycline concentration during the degradation of tetracycline by BiVO$_4$ (110)–Fe$_2$O$_3$. (f) Schematic diagram of the formation process of the electron transfer mechanism of Z-scheme heterojunctions. (g) Charge density difference diagram of BiVO$_4$ (110)–Fe$_2$O$_3$. Reproduced from ref. 156 with permission from Elsevier, copyright 2023.

including pollutant degradation,[150] formaldehyde (HCHO) removal,[151] and bacterial inactivation,[152] underscoring their importance in environmental remediation and the chemical industry.

4.2.1 Pollutant degradation. The rapid increase in global population and industrialization has led to a significant release of toxic antibiotics and dyes into the environment, causing severe pollution that threatens human health.[153] This necessitates the urgent development of effective technologies for pollutant degradation and environmental remediation. Photocatalytic technology has emerged as a promising, green method due to its cost-effectiveness and sustainability.[154] Under visible light irradiation, photocatalytic reactions demonstrate exceptional performance, where active electrons reduce O_2 to superoxide anions ($^\bullet O_2^-$), and photogenerated holes oxidize hydroxide ions (OH^-) to hydroxyl radicals ($^\bullet OH$). These reactive species effectively degrade specific organic pollutants, highlighting the potential of photocatalysis in environmental management. This section focuses on $BiVO_4$-based heterojunction photocatalysts for organic pollutant degradation, evaluating their effectiveness and prospects.

OVs are critical active sites in photocatalytic reactions, but their role in S-type heterojunctions requires further exploration. Su *et al.* constructed an S-type $BiVO_4$-s/g-C_3N_4 photocatalyst through interface modulation.[155] The Fermi level difference between $BiVO_4$ and g-C_3N_4 induces charge redistribution at the heterojunction interface, creating an IEF that enhances the transport and separation of photogenerated charge carriers. The introduction of OVs generates defect states within the E_g of $BiVO_4$, forming indirect recombination energy levels that mediate carrier recombination. Experimental results showed that the optimal sample enhanced photocatalytic efficiencies for degrading rhodamine B (RhB) and tetracycline (TC) by 10.7 (Fig. 8a) and 11.8 times (Fig. 8b), respectively, while the hydrogen production rate increased to 558 $\mu mol\ g^{-1}\ h^{-1}$ (Fig. 8c). This study highlights the importance of oxygen vacancies in heterojunction photocatalysis, providing insights for optimizing photocatalyst performance in environmental remediation and energy conversion.

The combined strategy of crystal facet engineering and Z-type heterojunction shows promise for addressing internal losses and carrier deficiencies in photocatalytic processes. Fu *et al.* selectively grew FeO nanoparticles on the (110) crystal facet of $BiVO_4$, creating a $BiVO_4$ (110)–FeO Z-type heterojunction for efficient TC degradation.[156] The study systematically examined the effects of catalyst dosage, pH, and temperature on degradation performance, revealing excellent catalytic activity, structural stability, and good reusability. In contrast, other studies have indicated that variations in pH can significantly alter the charge carrier dynamics and, consequently, the photocatalytic efficiency, emphasizing the need for a comprehensive understanding of these parameters across different systems. Under 60 min of visible light irradiation, the TC (15 mg L^{-1}) removal rates were 57.7% (Fig. 8d), 81.7%, and 91.5% (Fig. 8e) for the single-phase catalyst, non-directionally loaded $BiVO_4$–FeO, and directionally loaded $BiVO_4$(110)–FeO Z-type heterojunction (0.3 g L^{-1}), respectively. PEC testing and DFT calculations confirmed that the built-in electric field from $BiVO_4$ (110) to FeO(110) in the Z-type heterojunction facilitates effective separation and transport of photogenerated charge carriers, significantly enhancing photocatalytic degradation performance (Fig. 8f and g). The structures of intermediate products and their degradation pathways could provide valuable insights into photocatalytic reaction mechanisms. Comparative studies have shown that the efficiency of Z-type heterojunctions can vary widely based on the choice of co-catalyst and the specific structural characteristics of the heterojunction, underscoring the importance of tailored design in optimizing photocatalytic systems. A comparison of pollutant degradation performances of $BiVO_4$-based heterojunction photocatalysts is presented in Table 4.[28,31,157–167]

4.2.2 HCHO removal. HCHO is a common indoor pollutant with teratogenic and carcinogenic effects.[168] Photocatalytic technology offers an effective, eco-friendly solution for formaldehyde removal. Li *et al.* developed a $BiVO_4$/tubular g-C_3N_4

Table 4 Summary of the photocatalytic pollutant degradation performance of reported $BiVO_4$-based heterojunction photocatalysts

Photoelectrode design	Pollutant	Pollutant concentration	Catalyst dose (mg)	Time (min)	Light source	Photodegradation efficiency (%)	Ref.
$Cu_2O/BiVO_4$	Bisphenol A	20 mg L^{-1}	30	30	300 W Xe-lamp	65	31
$AgFeO_2$–$BiVO_4$	Ciprofloxacin	10 mg L^{-1}	100	30	300 W Xe-lamp	89.9	157
AgI/Cu–$BiVO_4$	Tetracycline	20 mg L^{-1}	30	30	300 W Xe-lamp	97.6	28
xNiCo$_2$O$_4$/$BiVO_4$	Rhodamine-B	20 ppm	50	150	450 W high-pressure mercury vapour lamp	91	158
F-$BiVO_4$/g-C_3N_4/CdS	Ciprofloxacin	20 mg L^{-1}	50	30	500 W Xe-lamp	98	159
$BiVO_4$/PANI	p-Nitrophenol	20 mg L^{-1}	50	20	500 W tungsten halogen lamps	98.25	160
$BiVO_4$/CoPc	Tetracycline	10 mg L^{-1}	20	10	300 W Xe-lamp	76	161
$BiVO_4$–$NiFe_2O_4$	Crystal violet dye	10 mg L^{-1}	100	60	250 W mixed metal halide lamp	95.65	162
Bi_2WO_6/$BiVO_4$	Rhodamine-B	10 mg L^{-1}	100	100	19 W blue LED	100	163
Fe/BiOCl/$BiVO_4$	Ciprofloxacin	10 mg L^{-1}	50	75	300 W Xe-lamp	100	164
g-C_3N_5/$BiVO_4$/CoFe–LDH-30%	Norfloxacin	10 mg L^{-1}	30	60	300 W Xe-lamp	95.3	165
Co–$BiVO_4$/Bi_2O_3	Chlortetracycline hydrochloride	30 mg L^{-1}	30	30	300 W Xe-lamp	90.5	166
KBr-g-C_3N_4/t-$BiVO_4$/m-$BiVO_4$	Ciprofloxacin	10 mg L^{-1}	40	240	300 W Xe-lamp	95.3	167

S-type heterojunction photocatalyst, achieving a formaldehyde removal efficiency of 90.7 $\pm$ 4.25% (Fig. 9a–d) under optimal conditions (light intensity of 2500 mW cm^{-2}, relative humidity of 40–60%, initial concentration of 0.2 mg m^{-3}, and catalyst loading of 3 g).[169] The S-type heterojunction enhances charge separation and redox capabilities. A semi-empirical equation was also developed to predict removal efficiency, highlighting catalyst loading and initial concentration as key factors. This heterojunction not only excels in formaldehyde removal but also provides a valuable reference for designing efficient photocatalysts.

4.2.3 Bacterial inactivation. Bacterial contamination is a major global health threat.[171] Photocatalysis, a non-toxic and efficient disinfection method, generates reactive species such as $^\bullet O_2^-$ and $^\bullet OH$ through the interaction of photogenerated electrons and holes with O_2 and H_2O, which destroy the bacterial cell membrane and cause cell death.[172] Lin *et al.* synthesized a Z-type BiVO$_4$/EAQ photocatalyst using a one-step water bath heating method, demonstrating its effectiveness in inhibiting electron–hole recombination and increasing the production of $^\bullet O_2^-$ and $^\bullet OH$.[170] After 150 min, the 60%-BiVO$_4$/EAQ composite achieved 100% inactivation efficiency against *S. flexneri* HL (Fig. 9c and d). The high charge separation efficiency and reduced recombination effects of the Z-type heterojunction were confirmed during a bacterial inactivation process. The photocatalytic process also resulted in the degradation of ARGs, further demonstrating the potential of photocatalytic technology in eliminating biological hazards.

5. Conclusions and perspectives

Photocatalysis is a highly innovative method for combating the growing issues of fossil fuel exhaustion and environmental contamination. Recent studies have highlighted the significant potential of BiVO$_4$-based heterojunction photocatalysts in both theoretical design and practical applications. Rational construction of heterojunctions is effective in achieving improved photocatalytic performance. Traditional heterojunctions and Schottky heterojunctions often show poor separation of photogenerated electrons and holes, or weak redox ability, resulting in limited photocatalytic efficiency. In contrast, Z-scheme heterojunctions and S-scheme heterojunctions are designed to enhance charge separation and maintain strong redox ability of catalysts, improving photocatalytic performance. Additionally, the diverse applications of BiVO$_4$-based heterojunction photocatalysts in energy and environmental fields, including water splitting, nitrogen fixation, CO$_2$ reduction, H$_2$O$_2$ synthesis, pollutant degradation, HCHO removal, and bacterial inactivation, demonstrate their wide-ranging potential. Future research could focus on optimizing photocatalyst structure and developing multifunctional catalysts that enhance activity through doping and co-catalyst integration. These photocatalysts demonstrate exceptional flexibility and stability in complex reaction systems, overcoming the limitations of single-reaction scenarios. Designing effective heterojunctions and improving reaction kinetics could enhance BiVO$_4$-based photocatalysts for energy conversion and environmental remediation. In view of this, we
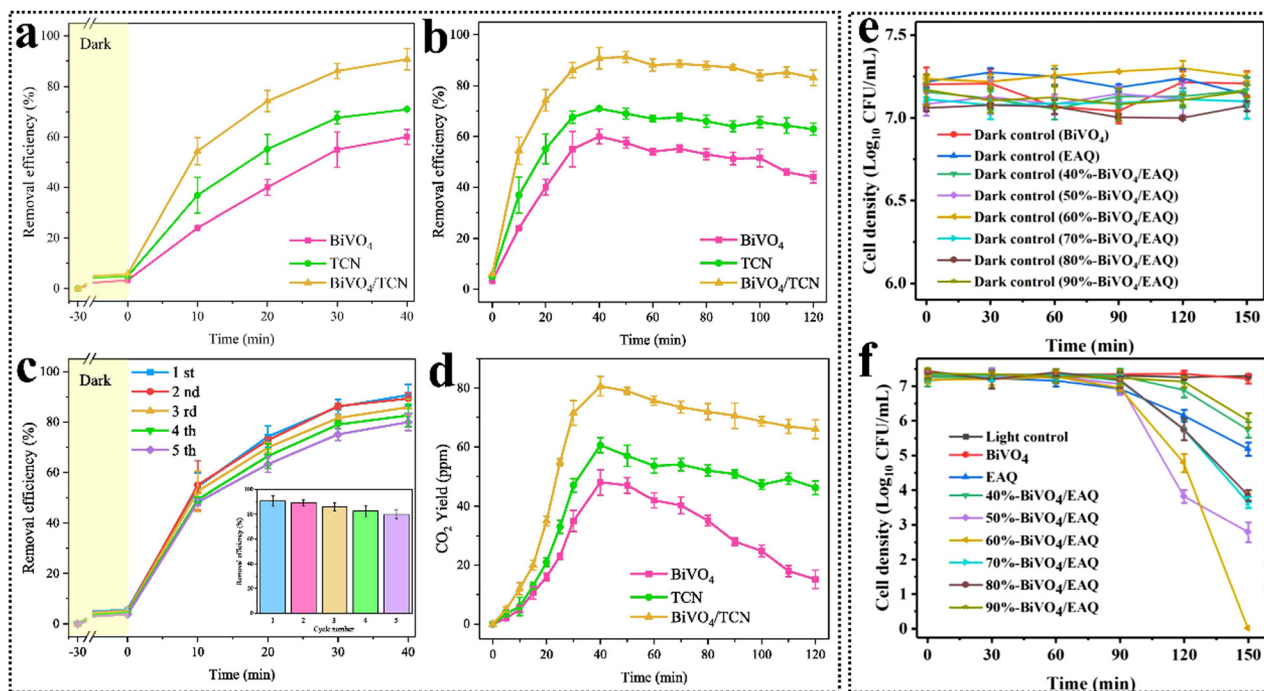
Fig. 9 Removal efficiency of HCHO by BiVO$_4$, TCN, and BiVO$_4$/TCN under light irradiation for (a) 40 min, and (b) 120 min. (c) Removal efficiency of HCHO with cycling test experiments by BiVO$_4$/TCN. (d) CO$_2$ yield under prolonged irradiation by BiVO$_4$, TCN, and BiVO$_4$/TCN during photocatalytic degradation of HCHO. Reproduced from ref. 169 with permission from Elsevier, copyright 2023. Effects of various photocatalysts on the survival cell density of *S. flexneri* HL with and without light irradiation ((e) in the dark and (f) under light irradiation). Reproduced from ref. 170 with permission from Elsevier, copyright 2023.

present some prospects for the development of BiVO$_4$-based heterojunction photocatalysts.

(1) Although BiVO$_4$-based heterojunction nanomaterials have been widely used for photocatalysis, challenges such as slow reaction kinetics must still be overcome to improve photocatalytic efficiency and stability. Combining BiVO$_4$ with other semiconductors (*e.g.*, PbS, WO$_3$) to form novel heterojunctions is expected to improve charge separation, reduce recombination rates and enhance overall performance.

(2) To further optimize charge transport in BiVO$_4$-based heterojunction catalysts, nanostructured BiVO$_4$ (*e.g.*, nanorods, nanosheets, or porous frameworks) can be fabricated to shorten the charge carrier diffusion length and increase the surface area for reactions. Additionally, introducing dopants (*e.g.*, Mo, W) or creating oxygen vacancies in the BiVO$_4$ lattice can enhance charge mobility and create localized energy states that facilitate charge separation and transport.

(3) Z-scheme and S-scheme heterojunctions enhance the separation and transfer of light-induced carriers while maintaining robust redox capabilities. Thus, these architectures can be explored in-depth, including the principles of excitation, transport, and recombination of photogenerated charge carriers, as well as the mechanism of photocatalytic reduction reactions.

(4) Given the complexity and diversity of heterojunction catalysts, designing and preparing a BiVO$_4$-based heterojunction with a controlled structure is challenging, and an understanding of the relationship between structure and performance is not yet sufficiently deep. Thus, integrating advanced tools such as artificial intelligence and DFT calculation can be well applied to deeply understand the mechanism of photocatalytic reactions and predict the performance of BiVO$_4$-based heterojunction catalysts.

(5) Advanced characterization techniques, such as high-resolution electron microscopy, and spectroscopic analysis, are suggested to better understand the mechanisms of BiVO$_4$-based heterojunctions and provide critical insights into material structures, defects, and charge transfer processes, aiding in performance optimization.

Data availability

The data that support the findings of this study are available from the corresponding author, FWQ, upon reasonable request.

Conflicts of interest

The authors declare no competing interests.

Acknowledgements

Notes and references

1 T. Zhang, L. Zhou, G. Chen, S. Xia and M. Qiu, *Chem. Commun.*, 2023, **59**, 1517–1520.
2 C. Yue, L. Chen, H. Zhang, J. Huang, H. Jiang, H. Li and S. Yang, *Environ. Sci.: Water Res. Technol.*, 2023, **9**, 669–695.
3 T. F. Qahtan, T. O. Owolabi, O. E. Olubi and A. Hezam, *Coord. Chem. Rev.*, 2024, **514**, 215839.
4 Z. Wang, X. Yue and Q. Xiang, *Coord. Chem. Rev.*, 2024, **504**, 215674.
5 D. Zu, H. Wei, Z. Lin, X. Bai, M. N. A. S. Ivan, Y. H. Tsang and H. Huang, *Adv. Funct. Mater.*, 2024, 2408213.
6 Y. Zhang, X. Wu, Z.-H. Wang, Y. Peng, Y. Liu, S. Yang, C. Sun, X. Xu, X. Zhang, J. Kang, S.-H. Wei, P. F. Liu, S. Dai and H. G. Yang, *J. Am. Chem. Soc.*, 2024, **146**, 6618–6627.
7 P. Li, R. Wu, P. Li, S. Gao, Z. Qin, X. Song, W. Sun, Z. Hua, Q. Wang and S. Chen, *Adv. Sci.*, 2024, 2408829.
8 A. M. Sadanandan, J.-H. Yang, V. Devtade, G. Singh, N. Panangattu Dharmarajan, M. Fawaz, J. Mee Lee, E. Tavakkoli, C.-H. Jeon, P. Kumar and A. Vinu, *Prog. Mater. Sci.*, 2024, **142**, 101242.
9 C. Chen, X. Zhang, E. Liu, J. Xu, J. Sun and H. Shi, *J. Mater. Sci. Technol.*, 2024, **198**, 1–11.
10 X. Hu, Z. Zhang, P. Lu, Y. Zhou, Y. Zhou, Y. Bai and J. Yao, *Water Res.*, 2024, **260**, 121936.
11 A. Fujishima and K. Honda, *Nature*, 1972, **238**, 37–38.
12 X. Xin, Y. Zhang, R. Wang, Y. Wang, P. Guo and X. Li, *Nat. Commun.*, 2023, **14**, 1759.
13 Q. Wu, J. Cao, X. Wang, Y. Liu, Y. Zhao, H. Wang, Y. Liu, H. Huang, F. Liao, M. Shao and Z. Kang, *Nat. Commun.*, 2021, **12**, 483.
14 G. N. Schrauzer and T. D. Guth, *J. Am. Chem. Soc.*, 1977, **99**, 7189–7193.
15 W. Zhao, Y. Li and W. Shen, *Chem. Commun.*, 2021, **57**, 6838–6850.
16 F. Xu, H. Tan, J. Fan, B. Cheng, J. Yu and J. Xu, *Solar RRL*, 2021, **5**, 2000571.
17 G. Liao, X. Tao and B. Fang, *Matter*, 2022, **5**, 377–379.
18 Y. Yang, J. Liu, M. Gu, B. Cheng, L. Wang and J. Yu, *Appl. Catal., B*, 2023, **333**, 122780.
19 G. Zhang, Y. Meng, B. Xie, Z. Ni, H. Lu and S. Xia, *Appl. Catal., B*, 2021, **296**, 120379.
20 B. Liu, X. Wang, Y. Zhang, K. Wan, L. Xu, S. Ma, R. Zhao, S. Wang and W. Huang, *Adv. Energy Mater.*, 2024, 2403835.
21 Y. Li, B. Bai, M. Zhu, J. Li, Q. Mei and Q. Wang, *J. Environ. Chem. Eng.*, 2024, **12**, 113079.
22 Y. Bai, Z. Fang, M. Zhai, X. Jiang, J. Li, H. Bai and W. Fan, *Chem. Commun.*, 2024, **60**, 6027–6030.
23 G. Zhao, J. Ding, F. Zhou, X. Chen, L. Wei, Q. Gao, K. Wang and Q. Zhao, *Chem. Eng. J.*, 2021, **405**, 126704.
24 C. Cheng, B. He, J. Fan, B. Cheng, S. Cao and J. Yu, *Adv. Mater.*, 2021, **33**, 2100317.
25 J. Gu, C. Ban, J. Meng, Q. Li, X. Long, X. Zhou, N. Liu and Z. Li, *Appl. Surf. Sci.*, 2023, **611**, 155575.
26 X. Qi, X. Zhu, J. Wu, Q. Wu, X. Li and M. Gu, *Mater. Res. Bull.*, 2014, **59**, 435–441.
27 J. Zhang, Y. Huang, X. Lu, J. Yang and Y. Tong, *ACS Sustainable Chem. Eng.*, 2021, **9**, 8306–8314.
28 J. Li, D. Wang, S. Zhao, R. Ma, J. Guo, Z. Li, D. Wang, Y. Xuan and L. Wang, *Appl. Catal., B*, 2024, **351**, 124007.
29 W. Xie, Z. Yu, H. Huang, R. Jiang, S. Yao, S. Huang, Y. Hou, S. Yin, R. Mo and C. Wu, *J. Colloid Interface Sci.*, 2024, **665**, 977–987.
30 U. Kumar, C.-X. Yang, Z.-Y. Deng, C.-E. Lin, B. C. Yadav and C.-H. Wu, *Sen. Actuators, B*, 2024, **403**, 135144.
31 C. Bai, W. Guo, Q. Liu, G. Li, S. Guo and R. Chen, *Appl. Catal., B*, 2024, **344**, 123606.
32 F. E. Osterloh, *Chem. Mater.*, 2008, **20**, 35–54.
33 A. Kubacka, M. Fernández-García and G. Colón, *Chem. Rev.*, 2012, **112**, 1555–1614.
34 T. F. Qahtan, T. O. Owolabi, O. E. Olubi and A. Hezam, *Coord. Chem. Rev.*, 2023, **492**, 215276.
35 F. Bhom and Y. M. Isa, *Glob. Chall.*, 2024, **8**, 2400134.
36 M. A. Ahmed and A. A. Mohamed, *RSC Adv.*, 2023, **13**, 421–439.
37 H. Wang, X. Gao, Y. Xie, E. Guo, H. Bai, F. Jiang, Q. Li and H. Yue, *Adv. Energy Mater.*, 2024, **14**, 2400493.
38 C. Hong, S. Oh, V. K. Dat, S. Pak, S. Cha, K.-H. Ko, G.-M. Choi, T. Low, S.-H. Oh and J.-H. Kim, *Light: Sci. Appl.*, 2023, **12**, 280.

39 C. Cui, X. Xu, X. Zhao, N. Xi, M. Li, X. Wang, Y. Sang, X. Yu, H. Liu and J. Wang, *Nano Energy*, 2024, **126**, 109632.

40 X. Rong, Y. Mao, J. Xu, X. Zhang, L. Zhang, X. Zhou, F. Qiu and Z. Wu, *Catal. Commun.*, 2018, **116**, 16–19.

41 J. Fan, M. Zuo, Z. Ding, Z. Zhao, J. Liu and B. Sun, *Chem. Eng. J.*, 2020, **396**, 125263.

42 X. Meng, S. Wang, C. Zhang, C. Dong, R. Li, B. Li, Q. Wang and Y. Ding, *ACS Catal.*, 2022, **12**, 10115–10126.

43 V. Devthade, A. Gupta and S. S. Umare, *ACS Appl. Nano Mater.*, 2018, **1**, 5581–5588.

44 Y. Zhu, T. Wan, X. Wen, D. Chu and Y. Jiang, *Appl. Catal., B*, 2019, **244**, 814–822.

45 K. Afroz, M. Moniruddin, N. Bakranov, S. Kudaibergenov and N. Nuraje, *J. Mater. Chem. A*, 2018, **6**, 21696–21718.

46 Y. Fang, Y. Ma and X. Wang, *Chin. J. Catal.*, 2018, **39**, 438–445.

47 J. S. Chang, Y. W. Phuan, M. N. Chong and J. D. Ocon, *J. Ind. Eng. Chem.*, 2020, **83**, 303–314.

48 Z. Zheng, X. Zu, Y. Zhang and W. Zhou, *Mater. Today Phys.*, 2020, **15**, 100262.

49 H. Wang, X. Yuan, H. Wang, X. Chen, Z. Wu, L. Jiang, W. Xiong and G. Zeng, *Appl. Catal., B*, 2016, **193**, 36–46.

50 Q. Xu, L. Zhang, B. Cheng, J. Fan and J. Yu, *Chem*, 2020, **6**, 1543–1559.

51 C. Pan, Z. Mao, X. Yuan, H. Zhang, L. Mei and X. Ji, *Adv. Sci.*, 2022, **9**, 2105747.

52 I. Ahmad, S. Shukrullah, M. Y. Naz, E. Ahmed, M. Ahmad, A. J. Obaidullah, A. Alkhouri, A. Mahal and Y. Y. Ghadi, *Mater. Sci. Semicond. Process.*, 2024, **172**, 108088.

53 P. K. Srivastava, Y. Hassan, Y. Gebredingle, J. Jung, B. Kang, W. J. Yoo, B. Singh and C. Lee, *ACS Appl. Mater. Interfaces*, 2019, **11**, 8266–8275.

54 H. Heng, Q. Gan, P. Meng and X. Liu, *J. Alloys Compd.*, 2017, **696**, 51–59.

55 J. Li, J. Chen, H. Fang, X. Guo and Z. Rui, *Ind. Eng. Chem. Res.*, 2021, **60**, 8420–8429.

56 J. Lin, T. Sun, M. Li, J. Yang, J. Shen, Z. Zhang, Y. Wang, X. Zhang and X. Wang, *J. Catal.*, 2019, **372**, 8–18.

57 Z. Ni, Y. Sun, Y. Zhang and F. Dong, *Appl. Surf. Sci.*, 2016, **365**, 314–335.

58 X. Wang, C. Zhang, J. Du, X. Dong, S. Jian, L. Yan, Z. Gu and Y. Zhao, *ACS Nano*, 2019, **13**, 5947–5958.

59 Y. Liu, H. Zeng, Y. Chai, R. Yuan and H. Liu, *Chem. Commun.*, 2019, **55**, 13729–13732.

60 M. Chang, M. Wang, M. Shu, Y. Zhao, B. Ding, S. Huang, Z. Hou, G. Han and J. Lin, *Acta Biomater.*, 2019, **99**, 295–306.

61 X. Wu, Y. Zhang, K. Wang, S. Zhang, X. Qu, L. Shi and F. Du, *J. Hazard. Mater.*, 2020, **393**, 122408.

62 A. Kumar, P. Choudhary, A. Kumar, P. H. C. Camargo and V. Krishnan, *Small*, 2022, **18**, 2101638.

63 B. P. Mishra and K. Parida, *J. Mater. Chem. A*, 2021, **9**, 10039–10080.

64 Y. Wang, X. Shang, J. Shen, Z. Zhang, D. Wang, J. Lin, J. C. S. Wu, X. Fu, X. Wang and C. Li, *Nat. Commun.*, 2020, **11**, 3043.

65 Q. Xu, S. Wageh, A. A. Al-Ghamdi and X. Li, *J. Mater. Sci. Technol.*, 2022, **124**, 171–173.

66 Q. Wang, T. Hisatomi, Y. Suzuki, Z. Pan, J. Seo, M. Katayama, T. Minegishi, H. Nishiyama, T. Takata, K. Seki, A. Kudo, T. Yamada and K. Domen, *J. Am. Chem. Soc.*, 2017, **139**, 1675–1683.

67 Q. Wang, J. Warnan, S. Rodríguez-Jiménez, J. J. Leung, S. Kalathil, V. Andrei, K. Domen and E. Reisner, *Nat. Energy*, 2020, **5**, 703–710.

68 X. Wu, G. Chen, L. Li, J. Wang and G. Wang, *J. Mater. Sci. Technol.*, 2023, **167**, 184–204.

69 K. Qi, B. Cheng, J. Yu and W. Ho, *Chin. J. Catal.*, 2017, **38**, 1936–1955.

70 H. Tada, T. Mitsui, T. Kiyonaga, T. Akita and K. Tanaka, *Nat. Mater.*, 2006, **5**, 782–786.

71 X. Zhou, Y. Xian, Z. Li, C. Yujie, J. Luo, X. Ning, X. Fan, Y. Zhong and X. Zhou, *Sep. Purif. Technol.*, 2025, **357**, 130117.

72 P. Wen, Y. Sun, H. Li, Z. Liang, H. Wu, J. Zhang, H. Zeng, S. M. Geyer and L. Jiang, *Appl. Catal., B*, 2020, **263**, 118180.

73 D. Huang, S. Chen, G. Zeng, X. Gong, C. Zhou, M. Cheng, W. Xue, X. Yan and J. Li, *Coord. Chem. Rev.*, 2019, **385**, 44–80.

74 F. Chen, Y. Wei, M. Ren, S. Sun, S. Ghosh and R. V. Kumar, *ChemCatChem*, 2024, **16**, e202301492.

75 P. Zhou, J. Yu and M. Jaroniec, *Adv. Mater.*, 2014, **26**, 4920–4935.

76 J. Fu, Q. Xu, J. Low, C. Jiang and J. Yu, *Appl. Catal., B*, 2019, **243**, 556–565.

77 J. Qu, D. Zhang, Y. Li, P. Wang, Y. Mao, T. Zhang, S. Zhan and Y. Li, *Appl. Catal., B*, 2024, **340**, 123246.

78 K. Qi, C. Imparato, O. Almjasheva, A. Khataee and W. Zheng, *J. Colloid Interface Sci.*, 2024, **675**, 150–191.

79 D. Zu, Y. Ying, Q. Wei, P. Xiong, M. S. Ahmed, Z. Lin, M. M. J. Li, M. Li, Z. Xu and G. J. A. C. I. E. Chen, *Angew. Chem. Int. Ed.*, 2024, **63**, 202405756.

80 M. Li, Z. Hu, D. Liu, Y. Liang, S. Liu, B. Wang, C. Niu, D. Xu, J. Li and B. Han, *Chem. Eng. J.*, 2024, **495**, 53519.

81 B. Borjigin, L. Ding, C. Liu, H. Li and X. Wang, *Chem. Eng. J.*, 2024, **485**, 149995.

82 L. Yuan, P. Du, L. Yin, J. Yao, J. Wang and C. Liu, *Nanoscale*, 2024, **16**, 5487–5503.

83 J. Zhou, B. Gao, D. Wu, C. Tian, H. Ran, W. Chen, Q. Huang, W. Zhang, F. Qi and N. J. A. F. M. Zhang, *Adv. Funct. Mater.*, 2024, **34**, 2308411.

84 H. Su, H. Yin, R. Wang, Y. Wang, W. Orbell, Y. Peng and J. Li, *Appl. Catal., B*, 2024, **348**, 123683.

85 M. A. Khan, S. Mutahir, I. Shaheen, Y. Qunhui, M. Bououdina and M. Humayun, *Coord. Chem. Rev.*, 2025, **522**, 216227.

86 C. Wang, Y. Ding, Y. Wang, Z. Xie, Z. Zeng, X. Li and Y. H. Ng, *Carbon Energy*, 2024, **6**, e500.

87 D. Pradhan, S. K. Biswal, R. Singhal, P. k Panda and S. K. Dash, *Surf. Interfaces*, 2024, **52**, 104954.

88 Y. Liu, C. Xing, Z. Yao, Q. Deng, T. Liang, S. Zhang, J. Pan, Z. Yu, T. Xie, R. Li and Y. Hou, *J. Colloid Interface Sci.*, 2025, **677**, 1095–1106.

89 Z. Wei, Y. Zhu, W. Guo, Q. Liu, W. Fang, Z. Jiang and W. Shangguan, *Appl. Catal., B*, 2020, **266**, 118664.

90 H.-Y. Luo, Z.-L. Liu, M.-R. Zhang, Y.-F. Mu and M. Zhang, *Nanoscale Adv.*, 2024, **6**, 1781–1789.

91 J. Bian, L. Sun, Z. Zhang, Z. Li, M. Chu, X. Li, D. Tang and L. Jing, *ACS Sustainable Chem. Eng.*, 2021, **9**, 2400–2408.

92 S. Shi, Y. Song, Y. Jiao, D. Jin, Z. Li, H. Xie, L. Gao, L. Sun and J. Hou, *Nano Lett.*, 2024, **24**, 6051–6060.

93 Y. An, C. Lin, C. Dong, R. Wang, J. Hao, J. Miao, X. Fan, Y. Min and K. Zhang, *ACS Energy Lett.*, 2024, **9**, 1415–1422.

94 S. Li, J. Liu, H. Wu, X. Zhang, Y. Guo, B. Kang and L. Zhao, *Int. J. Hydrogen Energy*, 2024, **84**, 739–758.

95 Y. Qi, B. Zhang, G. Zhang, Z. Zheng, T. Xie, S. Chen, G. Ma, C. Li, K. Domen and F. Zhang, *Joule*, 2024, **8**, 193–203.

96 S. Chaudhary, M. A. Hassan, M.-J. Kim, W.-G. Jung, J.-S. Ha, W.-J. Moon, S.-W. Ryu and B.-J. Kim, *Small Methods*, 2024, 2400794.

97 R. M. Sánchez-Albores, O. Reyes-Vallejo, F. Pola-Albores, A. Fernández-Madrigal, A. López-López and E. Ríos-Valdovinos, *J. Mater. Sci.: Mater. Electron.*, 2024, **35**, 1538.

98 Y. Gao, W. Fan, K. Qu, F. Wang, P. Guan, D. Xu, H. Bai and W. Shi, *New J. Chem.*, 2019, **43**, 8160–8167.

99 L. Li, Z. Zhang, D. Fang and D. Yang, *Inorg. Chem. Commun.*, 2024, **169**, 112971.

100 S. Xia, F. Xu and B. Weng, *J. Mater. Chem. A*, 2024, **12**, 4635–4642.

101 J.-W. Ji, L.-J. Zhang, H.-C. Wang, Y.-X. Duan, X.-Z. Yue, J.-H. Chen and S.-S. Yi, *Chem. Eng. J.*, 2024, **484**, 149597.

102 L. Shuai, L. Tian, X. Huang, J. Dou, J. Yu and X. Chen, *Int. J. Hydrogen Energy*, 2024, **88**, 19–28.

103 L. Wang, L. Ding, W. Zhai, S. Chu, J. Li, G. He, B. Wang and Z. Jiao, *Appl. Surf. Sci.*, 2024, **660**, 159963.

104 L. Liu, M. Ruan, C. Wang and Z. Liu, *ACS Appl. Electron. Mater.*, 2024, **6**, 4772–4782.

105 Q. Li, H. Chang, G. Gao, H. Jian, W. Liu, H. Jia, J. Xue, H. Liu and Q. Shen, *Sep. Purif. Technol.*, 2025, **353**, 128444.

106 A. Song, Y. Zhang, Z. Li and J. Hu, *Mater. Sci. Eng. B*, 2024, **302**, 117241.

107 D. Li, S. Tian, Q. Qian, C. Gao, H. Shen and F. Han, *Ind. Eng. Chem. Res.*, 2024, **63**, 13180–13188.

108 H. T. Htet, J. Yung, Y. Kim and S. Lee, *ACS Appl. Mater. Interfaces*, 2024, **16**, 52383–52392.

109 N. A. Mohamed, A. F. Ismail, T. S. Kiong and M. A. Mat Teridi, *Int. J. Hydrogen Energy*, 2024, **59**, 1063–1079.

110 Z. Xie, D. Chen, J. Zhai, Y. Huang and H. Ji, *Appl. Catal., B*, 2023, **334**, 122865.

111 J. Lin, X. Han, S. Liu, Y. Lv, X. Li, Y. Zhao, Y. Li, L. Wang and S. Zhu, *Appl. Catal., B*, 2023, **320**, 121947.

112 J. Li, Y. Wang, K. Sun, C. Cui, G. Zhong, W. Li, X. Yang, S. Liu, Z. Xing and M. Ma, *Next Energy*, 2024, **2**, 100056.

113 D. Yin, X. Ning, Q. Zhang, P. Du and X. Lu, *J. Colloid Interface Sci.*, 2023, **646**, 238–244.

114 D. Wang, J. Gu, H. Wang, M. Liu, Y. Liu and X. Zhang, *Appl. Surf. Sci.*, 2023, **619**, 156710.

115 S. Shen, R. Chen, X. Li, J. Wang, S. Yu, J. Li and F. Dong, *Environ. Sci. Technol.*, 2024, **58**, 7653–7661.

116 C. Zhang, J. Li, R. Chen, S. Shen, J. Wang, Y. Sun and F. Dong, *ACS Catal.*, 2024, **14**, 15721–15742.

117 M. A. Mushtaq, A. Kumar, G. Yasin, M. Tabish, M. Arif, S. Ajmal, W. Raza, S. Naseem, J. Zhao, P. Li, H. G. Ali, S. Ji and D. Yan, *Small*, 2024, **20**, 2310431.

118 Z. Shen, F. Li, L. Guo, X. Zhang, Y. Wang, Y. Wang, X. Jian, X. Gao, Z. Wang, R. Li, C. Fan and J. Liu, *Appl. Catal., B*, 2024, **346**, 123732.

119 Y. Zheng, E. Wang, J. Zhou and Z. Sun, *ACS Mater. Lett.*, 2024, **6**, 3572–3601.

120 K. Chen, R. Wang, Q. Mei, F. Ding, H. Liu, G. Yang, B. Bai and Q. Wang, *Appl. Catal., B*, 2024, **344**, 123670.

121 F. Wang, Q. Ding, Y. Bai, H. Bai, S. Wang and W. Fan, *Inorg. Chem. Front.*, 2022, **9**, 805–813.

122 F. Wang, Q. Ding, J. Ding, Y. Bai, H. Bai and W. Fan, *Chem. Eng. J.*, 2022, **450**, 138260.

123 Z.-L. Liu, H.-Y. Luo, M.-R. Zhang, Y.-F. Mu, F.-Q. Bai, M. Zhang and T.-B. Lu, *Chem. Eng. J.*, 2024, **491**, 151913.

124 G. Xia, Y. Meng, Q. Fu, Z. Huang, B. Xie, Z. Ni and S. Xia, *Chem. Eng. J.*, 2024, **498**, 155849.

125 Y. Bai, S. Gao, W. Xie, Z. Fang, H. Bai and W. Fan, *Int. J. Hydrogen Energy*, 2023, **48**, 10882–10890.

126 F. Hong, X. Su, Y. Fang, X. He and B. Shan, *J. Am. Chem. Soc.*, 2024, **146**, 25200–25210.

127 H. Bai, F. Wang, Q. Ding, W. Xie, H. Li, G. Zheng and W. Fan, *Inorg. Chem.*, 2023, **62**, 2394–2403.

128 Y. Bai, Z. Fang, Y. Lei, L. Liu, H. Zhao, H. Bai, W. Fan and W. Shi, *Green Energy Environ.*, 2024, **9**, 1112–1121.

129 G. Ren, Z. Zhao, Z. Li, Z. Zhang and X. Meng, *J. Catal.*, 2023, **428**, 115147.

130 R. Zha, C. Li, L. He and M. Zhang, *J. Colloid Interface Sci.*, 2022, **628**, 378–388.

131 Y. J. Yuan, N. Lu, L. Bao, R. Tang, F. G. Zhang, J. Guan, H. D. Wang, Q. Y. Liu, Q. Cheng, Z. T. Yu and Z. Zou, *ACS Nano*, 2022, **16**, 12174–12184.

132 D. Zhang, S. Yang, X. Fang, H. Li, X. Chen and D. Yan, *Chin. Chem. Lett.*, 2022, **33**, 4669–4674.

133 G. Zhang, X. Yuan, B. Xie, Y. Meng, Z. Ni and S. Xia, *Chem. Eng. J.*, 2022, **433**, 133670.

134 C. Zhu, J. Cheng, H. Lin, Z. Yang, Y. Huang, F. Lv, H. Bai and S. Wang, *J. Am. Chem. Soc.*, 2024, **146**, 24832–24841.

135 M. Ahmadi, S. M. Alavi and A. Larimi, *Surf. Interfaces*, 2024, **45**, 103908.

136 Z. Zhao, J. Bian, L. Zhao, H. Wu, S. Xu, L. Sun, Z. Li, Z. Zhang and L. Jing, *Chin. J. Catal.*, 2022, **43**, 1331–1340.

137 J. Wu, L. Xiong, Y. Hu, Y. Yang, X. Zhang, T. Wang, Z. Tang, A. Sun, Y. Zhou, J. Shen and Z. Zou, *Appl. Catal., B*, 2021, **295**, 120277.

138 Y. Deng, J. Wang, J. Wang, W. Wang, H. Zhang and S. Yin, *Chem. Eng. J.*, 2024, **496**, 153963.

139 N. Saini, S. Saini, S. Majumder, K. S. Campbell and S. L. Jain, *Sustainable Energy Fuels*, 2024, **8**, 1750–1760.

140 Z. He, Y. Liu, Z. Li, S. Xu, Z. Li, J. Bian and L. Jing, *Appl. Catal., B*, 2024, **355**, 124207.

141 R. Chen, Q. Wang, G. Gao, L. Wu and J. Luo, *ACS Catal.*, 2024, **14**, 12234–12241.

142 M. Xie, Q. Xu, T. Lv and H. Liu, *J. Alloys Compd.*, 2024, **977**, 173342.

143 X. Liu and Z. Lou, *Appl. Surf. Sci.*, 2025, **680**, 161328.

144 Z. Li, B. Liu, X. Zhang, C. Zhang, Y. Bai, J. Liu, Y. Wang, S. Yang, R. Li and C. Fan, *Sustainable Energy Fuels*, 2024, **8**, 262–271.

145 V. Liapun, M. B. Hanif, M. Sihor, X. Vislocka, S. Pandiaraj, V. K. Unnikrishnan, G. K. Thirunavukkarasu, M. F. Edelmannová, M. Reli, O. Monfort, K. Kočí and M. Motola, *Chemosphere*, 2023, **337**, 139397.

146 C. Chen, M. Wu, Y. Xu, C. Ma, M. Song and G. Jiang, *J. Am. Chem. Soc.*, 2024, **146**, 9163–9171.

147 P. Tan, R. Ren, L. Yang, M. Zhang, H. Zhai, H. Liu, J. Chen and J. Pan, *J. Mol. Liq.*, 2024, **393**, 123644.

148 B. Huang, X. Fu, K. Wang, L. Wang, H. Zhang, Z. Liu, B. Liu and J. Li, *Adv. Powder Mater.*, 2024, **3**, 100140.

149 J. Huang, H. Shi, X. Wang, P. Wang, F. Chen and H. Yu, *Catal. Sci. Technol.*, 2024, **14**, 2514–2521.

150 Y. Gao, F. Liu, X. Chi, Y. Tian, Z. Zhu, R. Guan and J. Song, *Appl. Surf. Sci.*, 2022, **603**, 154416.

151 Z. Jiang, T. Wang, J. Wang, T. Yu, C. Kong, Z. Yang and H. Zhu, *Sep. Purif. Technol.*, 2025, **353**, 128581.

152 S. Bao, Z. Wang, J. Zhang and B. Tian, *ACS Appl. Nano Mater.*, 2020, **3**, 8604–8617.

153 Z. Ciğeroğlu, N. El Messaoudi, Z. M. Şenol, G. Başkan, J. Georgin and S. Gubernat, *Mater. Today Sustainability*, 2024, **26**, 100735.

154 J. Yang, S. Tian, Z. Song, Y. Hao and M. Lu, *Coord. Chem. Rev.*, 2025, **523**, 216257.

155 K. Su, L. Zheng, M. Liu, J. Gao, Z. Shi, C. Chen, Y. Li, J. He and M. Peng, *Small*, 2024, 2405551.

156 Q. Fu, Y. Meng, Y. Yao, H. Shen, B. Xie, Z. Ni and S. Xia, *J. Environ. Chem. Eng.*, 2023, **11**, 111060.

157 Q. Ma, J. Ren, X. Sun, X. Chen, G. Liu, S. Wang and H. Yang, *Appl. Surf. Sci.*, 2025, **679**, 161275.

158 N. D. Kolhe, L. S. Walekar, A. N. Kadam, M. A. Kulkarni, H. A. Parbat, M. Misra, B. J. Lokhande, S. W. Lee, V. Patil, D. Mhamane and M. G. Mali, *Chemosphere*, 2024, **352**, 141353.

159 Z. Yang, J. Yang, L. Li, W. Cao, J. Zhang, H. Zhao and L. Wang, *Appl. Surf. Sci.*, 2024, **672**, 160738.

160 T. Jiteshwaran, B. Janani, A. Syed, A. M. Elgorban, I. Abid, L. S. Wong and S. S. Khan, *Surf. Interfaces*, 2024, **49**, 104361.

161 Z. Long, X. Zheng and H. Shi, *Sci. Chin. Mater.*, 2024, **67**, 550–561.

162 R. C. Ghaware, N. B. Birajdar, G. S. Kamble and S. S. Kolekar, *Langmuir*, 2024, **40**, 14426–14439.

163 S. J. Segovia-Sandoval, E. Mendoza-Mendoza, A. Jacobo-Azuara, B. A. Jiménez-López and A. C. Hernández-Arteaga, *Environ. Sci. Pollut. Res.*, 2023, **31**, 39945–39960.

164 G. Yu, Q. Sun, Y. Yang, S. Chen, Y. Long, Y. Li, S. Ge and D. Zheng, *Prog. Nat. Sci.: Mater. Int.*, 2024, **34**, 290–303.

165 E. Lee, G. Jagan, J. U. Choi, B. Cha, Y. Yoon, K. Saravanakumar and C. M. Park, *Chem. Eng. J.*, 2024, **494**, 152961.

166 Y. Gao, Y. Hu, F. Liu, Y. Tian, D. Zeng, T. Shen, H. Yuan, R. Guan and J. Song, *Ceram. Int.*, 2024, **50**, 5643–5656.

167 P. Chen, X. Ou, C. Xia, K. Wang, M. Zhang, M. Wei and Y. Wang, *Sep. Purif. Technol.*, 2024, **349**, 127866.

168 S. Suresh and T. J. Bandosz, *Carbon*, 2018, **137**, 207–221.

169 Y.-W. Li, S.-Z. Li, M.-B. Zhao and W.-L. Ma, *Sep. Purif. Technol.*, 2023, **327**, 124966.

170 Z. Lin, S. Ye, Y. Xu, X. Lin, Z. Qin, J. Bao and H. Peng, *Chem. Eng. J.*, 2023, **453**, 139747.

171 E. Belykh, T. Maystrenko, I. Velegzhaninov, M. Tavleeva, E. Rasova and A. Rybak, *J. Microorganisms*, 2024, **12**, 733.

172 B. Xue, L. Tian, Y. Liu, L. Peng, W. Iqbal, L. Li and Y. Mao, *Environ. Sci. Ecotechnology*, 2024, **21**, 100390.